Theoretical and Applied Fracture Mechanics 147 (2026) 105832

Contents lists available at ScienceDirect

Theoretical and Applied Fracture Mechanics

journal homepage: www.elsevier.com/locate/tafmec

TCD–statistics–machine learning framework for defect-controlled fatigue in recycled powder LPBF Inconel 718

L. Romanelli [a,*], C. Santus [b], G. Macoretta [b], B.D. Monelli [b], H. Rajaei [a], C. Menapace [a], M. Benedetti [a,*]

[a] *Department of Industrial Engineering, University of Trento, Trento, Italy*
[b] *Department of Civil and Industrial Engineering, University of Pisa, Pisa, Italy*

ARTICLE INFO

Keywords:
Laser powder bed fusion
Inconel 718
Recycled powder
Theory of critical distances
Defects
Surrogate models
Size effect

ABSTRACT

Additive manufacturing (AM) represents a promising route towards more resource-efficient production of high-performance metallic components. However, the reliable assessment of fatigue behaviour in the presence of process-induced defects remains a major challenge, particularly for defect-sensitive alloys such as laser powder bed fusion (LPBF) Inconel 718. This work proposes a fatigue modelling framework integrating the Theory of Critical Distances (TCD), extreme value statistics (EVS), finite element (FE) simulations, and computational surrogate models (CSMs) to quantify the combined influence of surface roughness, internal porosity, macro-notches and size effect on fatigue strength. The methodology was validated using plain and V-notched LPBF Inconel 718 specimens manufactured from two partially recycled powder feedstocks. Surface topography was characterized through profilometry, while metallographic analyses were employed to determine pore size and location distributions. FE simulations were used to evaluate fatigue stress concentration factors (FSCFs) of surface roughness, and a surrogate model, based on FE simulation results, was used to calculate FSCFs of pores. The proposed computational framework enabled us to obtain high correlation factor $R^2 \approx 0.90$ and low symmetric mean absolute percentage error SMAPE $\approx$ 17.8%, through FSCFs at 99th percentile, while FSCFs at 95th percentile provided $R^2 \approx 0.65$ and SMAPE $\approx$ 34.2%. The numerical results also confirmed the fractographic evidence that surface roughness was the primary crack initiation site, with roughness-related FSCFs about 25% higher than pore-related ones. The proposed approach offers a computationally efficient engineering methodology for defect-driven fatigue assessment of additively manufactured metallic components under LPBF conditions dominated by near-spherical gas porosity.

1. Introduction

The transition towards a circular and resource-efficient manufacturing economy is pushing industrial sectors to reconsider how metallic components are produced, used, and recycled. Inconel 718, a nickel-based superalloy widely employed in aerospace, energy, and transportation sectors [1], is particularly attractive for such efforts due to its high critical raw-material content and the significant environmental burden associated with producing conventional atomized powders. Traditional manufacturing routes for high-performance alloys, such as Inconel 718, are energy-intensive and generate substantial quantities of scrap—often exceeding 40% of processed mass in aerospace and power-generation applications [2]. Recent life-cycle assessments consistently identify powder atomization and upstream alloy preparation as dominant contributors to the carbon footprint of metal additive manufacturing (AM), often accounting for 25%–40% of the total embodied energy of AM components [3]. These findings highlight the strategic importance of developing sustainable powder feedstocks to unlock the full environmental potential of AM. Within this framework, two complementary circular approaches are emerging: (i) powder reuse within laser powder bed fusion (LPBF) systems and (ii) regeneration or re-atomization of solid scrap into AM-grade powder. Powder reuse is widely adopted industrially but induces progressive physicochemical changes. Repeated thermal exposure, spatter incorporation, and oxidation alter particle size distribution (PSD), surface chemistry and flowability, potentially reducing powder bed density and increasing defect susceptibility. A recent comprehensive review [4] highlights that degradation mechanisms, such as oxide thickening, satelliting, and compositional drift, may affect mechanical reliability, particularly in fatigue-sensitive applications. While several alloys tolerate

* Corresponding authors.
E-mail addresses: lorenzo.romanelli-1@unitn.it (L. Romanelli), matteo.benedetti@unitn.it (M. Benedetti).

https://doi.org/10.1016/j.tafmec.2026.105832
Received 14 May 2026; Received in revised form 9 July 2026; Accepted 20 July 2026
Available online 1 August 2026

Nomenclature

AM	Additive manufacturing
FE	Finite element
TCD	Theory of critical distances
CSM	Computational surrogate model
ANN	Artificial neural network
FSCF	Fatigue stress concentration factor
LPBF	Laser powder bed fusion
BD	Build direction
EVS, GEV	Extreme value statistics and generalized extreme value
PSD	Particle size distribution
SEM	Scanning electron microscope
PDF	Probability distribution function
R_{N}	Nominal notch radius of V-notched specimens
d_{N}	Net diameter of V-notched specimens
D_{G}	Gross diameter of V-notched specimens
VR1	V-notched specimen with nominal notch radius equal to 1 mm
VR03	V-notched specimen with nominal notch radius equal to 0.3 mm
AB	As-built
HT	Heat treated
PM	Point method
LM	Line method
SMAPE	Symmetric mean absolute percentage error
$\sqrt{area}$	Square root of area of internal defects according to the Murakami model
P	Laser power
v	Scan velocity
h	Hatch distance
t	Layer thickness
A_{r}	Meltpool aspect ratio
B_{r}	LPBF build rate
E	Young modulus
S_{Y}	Yield strength
S_{U}	Ultimate strength
eR	Elongation at fracture
AR	Area reduction
$\mathrm{HV}_{\mathrm{av,v}}$, $\mathrm{HV}_{\mathrm{av,c}}$, $\mathrm{HV}_{\mathrm{av,F}}$	Average value of Vickers hardness of virgin, cyclone and Fenice specimens
σ_{HV}	Standard deviation of measured Vickers hardness
R	Stress ratio of the fatigue tests
σ_{a}	Stress amplitude
$\sigma_{\mathrm{a,c}}$, $\sigma_{\mathrm{a,F}}$	Stress amplitude of cyclone and Fenice specimens
N_{f}	Number of cycles to failure
k, b	Basquin law parameters
N, q	Number of experimental data and parameters of the fitted curve
σ_{f}	Standard deviation of the fitted SN curves
OM	Optical microscope
f_{s}	Pores shape factor
$Area$, P	Area and perimeter of pores
R_{a}	Roughness parameter for the average absolute deviation of the profile from the mean line
D	Maximum pore diameter obtained from each scan
d	Distance of pore with maximum diameter from external surface
F_{V}, F_{G}, F_{E}	Generalized extreme value, EVS (Gumbel) and exponential distributions
a, b	Parameters of EVS
μ_{gev}, σ_{gev}, ζ	Parameters of GEV
μ	Parameter of exponential distribution
V_0, S_0	Reference volume and surface according to Murakami approach
L	Critical distance according to line method
σ_{a}^*	Intrinsic fatigue strength
A, B	Parameters of the power law describing the dependence between L and N_{f}
σ_x	Axial stress
σ_{u}	Unitary stress used for FSCF calculation
$\sigma_{x,\mathrm{V}}$	Axial stress obtained through 2D FE simulations of the only notch
$\sigma_{x,\mathrm{V,pore}}$	Axial stress obtained through 3D FE simulations with the pore and the notch
$\mathcal{L}$, $\mathcal{L}'$	Loss functions of the developed surrogate models
y_i, $\hat{y}_i$	Target and predicted values in surrogate models
$y_{i,\mathrm{min}}$, $y_{i,\mathrm{max}}$	Minimum and maximum imposed physical constraints on output values of surrogate model
λ	Weight factor of surrogate model to balance between MSE and physical constraints
HSS, HSV	Highly-stressed surface and highly-stressed volume
h_{p}	Distance of deepest valley from mean surface profile
$K_{\mathrm{f,rough}}$, $K_{\mathrm{f,pore}}$	FSCFs provided by surface roughness and pores
$K_{\mathrm{f,pl,pore}}$, $K_{\mathrm{f,V,pore}}$	FSCFs provided by pores in plain and V-notched specimens
$K_{\mathrm{f,pl,rough}}$, $K_{\mathrm{f,V,rough}}$	FSCFs provided by surface roughness in plain and V-notched specimens
$K_{\mathrm{f,hard}}$	Degradation effect caused by the reduction of HV with respect to virgin specimens
δ_i	Borgonovo index
f_{Y}	PDF of the output of the ANN
$f_{\mathrm{Y}\vert x_i}$	PDF of the output of the ANN given a fixed input x_i
n_k	Number of data points in each bin during the calculation of Borgonovo indices
α	Size ratio
K_{f} (99%)	FSCF at 99th percentile
K_{f} (95%)	FSCF at 95th percentile
$K_{\mathrm{f,tot}}$	Total FSCF combining the effects of pores, surface roughness and hardness decrease
$\mathrm{E}_{\mathrm{Log.},i}$	Logarithmic error for N_{f}

multiple reuse cycles under controlled sieving and rejuvenation strategies, defect-sensitive materials require careful evaluation of powder evolution and its impact on structural integrity [5]. Beyond in-situ reuse, recycling of solid metallic scrap into new AM-grade powders has recently demonstrated promising environmental benefits [6–8]. Gas atomization of mixed industrial scrap into Al-based LPBF feedstock reduced carbon footprint by approximately 50% compared to virgin powder [9,10]. For example, waste-derived Inconel 725 powders processed by LPBF achieved relative densities up to 99.99% within a broad process window, confirming technical feasibility of scrap-based nickel superalloys [11]. Advanced regeneration approaches such as ultrasonic plasma atomization further enable upcycling of degraded powders, restoring sphericity and reducing cradle-to-gate energy demand by approximately 50% relative to virgin feedstock [3]. From a circular economy perspective, powder-bed processes inherently support high material recovery rates (80%), but full sustainability integration requires ensuring that recycled feedstocks preserve mechanical reliability [12]. A substantial body of research confirms both the technical feasibility and environmental benefits of using recycled metallic feedstocks in AM [10,13]. Early demonstrations on nickel-based alloys showed that dense, structurally sound Inconel 718 components can be produced from gas-atomized recycled scrap, achieving tensile strengths comparable to, and in some cases exceeding, those obtained from virgin powder [14,15]. These studies demonstrate that recycled or partially recycled powders can meet the stringent morphological, chemical, and rheological requirements of LPBF. Despite these advances, most sustainability-oriented studies focus primarily on density, tensile strength, and hardness. The influence of recycled or scrap-derived powders on fatigue performance remains insufficiently understood, particularly for defect-sensitive alloys such as LPBF Inconel 718. Fatigue strength in this material is governed by surface roughness, internal defects and notch sensitivity [6]. These factors may be influenced, directly or indirectly, by the origin and processing history of the powder feedstock. Accordingly, systematic investigations of defect populations, their statistical distributions, and their interaction with local stress fields are essential to establish reliable fatigue predictions for components manufactured from sustainable powder feedstocks.

It is widely recognized that the fatigue behaviour of AM Inconel 718 is dominated by surface morphology and internal defects, which act as severe stress raisers and preferential crack-initiation sites [16–18]. Rough as-built (AB) surfaces, resulting from layered melt-pool solidification and partially fused powder particles, create micro-notches whose amplitude and spacing strongly affect fatigue strength [19]. Macoretta et al. [20] demonstrated that surface roughness can impose a fatigue debit comparable to that of internal defects, and other studies confirm that fatigue performance degrades significantly with increasing roughness amplitude, skewness, and kurtosis, highlighting the importance of quantitative topographical characterization for AM surfaces [21,22]. These findings are consistent with broader fatigue studies on AM Inconel 718. A recent review by Alfred and Amiri [23] emphasized that surface condition is a dominant factor governing crack initiation across different fatigue life regimes, with process-induced roughness regularly identified as the primary origin of micro-cracks. Self-heating fatigue experiments further confirm the critical role of surface morphology as demonstrated by Matušů et al. [24]. Improvements in surface finish can therefore yield substantial gains in fatigue strength. In hybrid LPBF systems employing in-situ high-speed milling, Sommer et al. [25] reported significant increases in endurance limit for surfaces with $R_a \approx 1$ μm, demonstrating that even moderate reductions in roughness amplitude can meaningfully delay crack nucleation. Profilometers can provide valuable sustain through the analysis of surface profiles as described in [26,27], and they are often used to collect useful information about surface topography.

Internal defects, such as lack-of-fusion flaws, gas-induced spherical pores and keyhole porosity, represent another factor influencing crack initiation in AM metals [28–30]. Their harmfulness depends not only on size, shape, and morphology but also on depth relative to the free surface, with subsurface pores within ≈100–200 μm often exhibiting the greatest fatigue sensitivity [31]. Romanelli et al. [32] showed that extreme value statistics (EVS) is essential to capture the rare but highly detrimental defects controlling fatigue strength, consistent with classical defect-dominated fatigue models. Recent studies on porosity formation and process monitoring further underscore the complexity of internal defects. Bostan et al. [29] demonstrated that pores arise from multiple interacting mechanisms, including localized lack of fusion, keyhole instability and spatter-induced layer perturbations, and that their morphology is highly sensitive to thermal history and scan strategy. Their infrared-based monitoring showed that even under optimized conditions, small but harmful pores (<50 μm) may persist. Energy-based fatigue analyses further showed that variations in defect populations lead to large differences in high-cycle/very high-cycle fatigue behaviour and that accurate predictions require explicit consideration of micro-defect distributions rather than reliance on smooth-specimen S–N curves [33]. Collectively, these insights establish that fatigue performance of LPBF Inconel 718 depends primarily on defect populations, regardless of whether powders originate from virgin or recycled sources.

Several modelling approaches have been adopted to capture defect-driven fatigue in AM specimens. The Murakami $\sqrt{area}$ parameter provides a unifying descriptor for both surface and internal defects [34–38]. Recent AM studies refine this concept using profilometry-derived defect metrics and EVS to estimate the critical $\sqrt{area}$ driving fatigue failure [39,40]. Other methods were used such as finite fracture mechanics [41,42], strain energy density [43–45] or strain-based finite fracture mechanics proposed by Mirzaei et al. in [46]. According to this latter, two conditions must be satisfied such as the non-local strain requirement and the energy balance. The strain and the stress intensity factors at failure were used as input for calibrating the model, which was then validated on U- and V-notched specimens obtaining a good overlap with the experimental results. Alternatively, the Theory of Critical Distances (TCD) offers another physically grounded framework, incorporating a material-specific characteristic length that governs sensitivity to stress gradients near defects [47–49]. Considering the explanatory example of a notched component under uniaxial loading, TCD-Line method (LM) identifies the effective stress by averaging the uniaxial stress distribution along the notch bisector over the distance $2L$, where L is the critical distance, while point method (PM) calculate effective stress by evaluating the stress at distance $L'/2$ from notch apex. TCD was also formulated in terms of area and volume methods where the stress distributions are averaged over areas and volumes, respectively, and it was also combined with critical plane criteria as in [50,51]. After having widely demonstrated a strong ability to capture the effects of stress raisers in specimens manufactured through traditional technologies [52–60] under different loading scenarios, fibre composite laminate materials [61], industrial mechanical components such as spur gears [62], contact mechanics fretting fatigue [63,64] and different types of rocks [65], TCD has proven to be highly effective for AM components, both polymeric and metallic, under both static and fatigue loading scenarios [66–71]. FE simulations are generally implemented to calculate the stress distributions used in TCD.

Although FE modelling provides accurate stress fields around pores and notches, its direct application in large-scale probabilistic fatigue assessments is limited by the associated computational cost. Computational surrogate models (CSMs), such as neural-based architectures, offer an efficient alternative: once trained on suitably sampled FE simulations or adequate formulas or experimental data, CSMs can rapidly predict fatigue strength for arbitrary combinations of defect size, depth, shape [72,73]. Combined with statistically characterized defect distributions, CSMs enable the generation of synthetic defect populations, tens or hundreds of thousand, facilitating robust estimation of high-percentile fatigue stress concentration factors (FSCFs). Several CSMs were implemented in the field of AM such as the work of Karolczuk and Kurek [74] about Gaussian process to identify the impact of mean stress components and dominant damage mechanisms in LPBF maraging specimens under different multiaxial loading scenarios [74], that of Salvati et al. [75] where a physics-informed neural network,

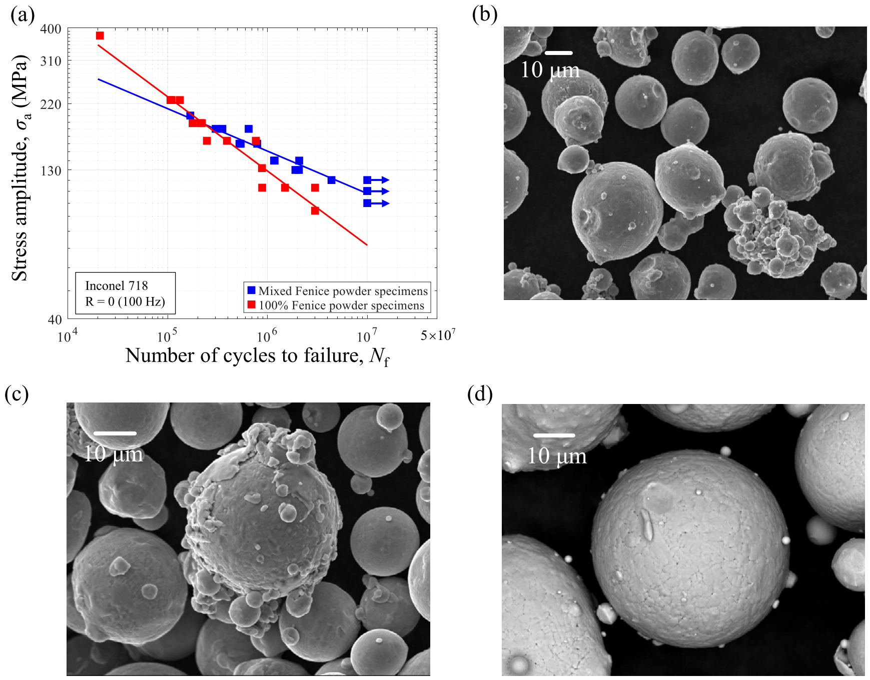

Fig. 1. (a) Comparison between SN curves of mixed Fenice and 100% Fenice powder specimens and SEM images of the different types of powder: (b) virgin [32], (c) cyclone and (d) Fenice.

combining linear elastic fracture mechanics methods and defects characteristics, was implemented to predict uniaxial fatigue strength of AlSi10Mg AM specimens under uniaxial loadings and that of Centola et al. [76] where a Bayesian neural network was developed to evaluate the combined effects of building orientation, laser power, scan speed, hatch distance and layer thickness on the fatigue strength of LPBF 316L. At the defect-detection level, Perghem et al. [77] demonstrated that CSMs-enhanced X-ray computed tomography segmentation significantly improves defect-classification accuracy, particularly for fragmented lack-of-fusion defects, thereby providing more reliable defect statistics for fatigue modelling.

Despite the potential of the above-mentioned algorithms to model, through FE simulations or analytical expressions or CSMs techniques, the effects of surface roughness and internal defects on the fatigue strength of AM materials, the literature lacks a unified approach to account for the combined impact of size effect, surface roughness, internal defects and macro-notches on the fatigue strength of AM materials. In order to address this open research question, this work proposes a novel unified hybrid methodology integrating TCD, statistical modelling, FE simulation, and CSMs to quantify the combined influence of surface roughness, internal porosity, notches, and size effect on the fatigue strength of AM components, of different geometries, manufactured through LPBF and recycled powder feedstocks. Surface topographies were captured via profilometer, the morphologies of the pores were extracted through metallographic analyses, and defect populations were modelled using EVS. Roughness-driven FSCFs were computed using FE, TCD-LM and EVS. Two types of CSMs, i.e. a classical artificial neural network (ANN) and an additional neural network with physical constraints embedded in the loss function, were trained on 3D FE simulations for predicting pore-induced FSCFs across a wide defect-parameter space, supporting the generation of a ≈100 000-defect synthetic population. The impact of uncertainty of input parameters on output results of the ANN was evaluated through Borgonovo indices. The size effect was then introduced to calculate the FSCFs of pores and surface roughness at 99th and 95th percentiles, and the FSCFs of pores and surface roughness were conservatively combined for fatigue strength predictions and the results obtained at 95th and 99th percentiles were compared. Finally, a range of validity of the proposed computational approach was also presented. The proposed framework is proposed intending LPBF process conditions where parameter optimization minimizes lack-of-fusion defects and the defect population is dominated by near-spherical gas-induced porosity. Under these conditions, continuum-scale modelling combined with metallographic characterization provides a robust engineering description of defect-driven fatigue behaviour. The framework was intentionally developed to retain computational tractability for large defect populations and engineering fatigue assessment workflows. The strong agreement between predictions and experiments demonstrates the effectiveness of integrating FE, TCD, EVS and CSMs for fatigue assessment of AM components, including those produced from recycled powder feedstocks, under the above mentioned conditions.

2. Experimental investigations

2.1. Powder characterization

Two different powder feedstocks were employed for specimens manufacturing, both obtained by blending 50 wt% virgin Inconel 718 powder with 50 wt% powder from sustainable sources. The first feedstock, hereafter referred to as cyclone, was obtained by recovering the powder collected by the cyclonic separator of the Renishaw RenAM 500S Flex LPBF machine at the University of Pisa. This unit extracted entrained powder particles and solidified spatter droplets transported from the processing chamber by the recirculating argon gas stream. The material was collected while the machine was processing virgin Inconel 718 powder. The powder was sieved using a 63 µm mesh in an argon-filled chamber. The second feedstock, termed Fenice and supplied by F3nice srl (Italy), was obtained by atomizing Inconel 718 scrap material. In contrast to the approach adopted in [3], the present study sought to further advance upcycling strategies by extending the recycled feedstock not only to bulky scrap but also to machining chips, with a feedstock composition of 75 wt% bulk scrap and 25 wt% chips. The decision to blend both sustainable powders with virgin material was motivated by experimental evidence, summarized in Fig.

Table 1
Percentages of the chemical elements in virgin [32], sieved cyclone and Fenice Inconel 718 powders.

Type of powder	Cr	Ni	Fe	Mo	Nb	Ti	Al	C	Mn	Si	Co	Cu	O
Virgin	18.7	52.7	18.6	3.1	4.99	0.98	0.44	0.059	0.06	0.14	0.03	0.02	<0.01
Cyclone	18.9	53.0	17.8	3.16	5.1	1.03	0.50	0.02	0.05	0.006	0.05	0.01	<0.01
Fenice	18.1	54.5	17.1	2.93	4.95	0.93	0.50	0.03	0.09	0.009	0.05	0.05	<0.01

Table 2
Ratios of Cr, Fe, Mo, Nb, Ti and Al to Ni in virgin [32], sieved cyclone and Fenice Inconel 718 powder.

Type of powder	Cr/Ni (%)	Fe/Ni (%)	Mo/Ni (%)	Nb/Ni (%)	Ti/Ni (%)	Al/Ni (%)
Virgin	35.5	35.3	5.88	9.47	1.86	0.83
Cyclone	35.7	33.6	5.96	9.62	1.94	0.94
Fenice	33.2	31.4	5.38	9.08	1.71	0.92

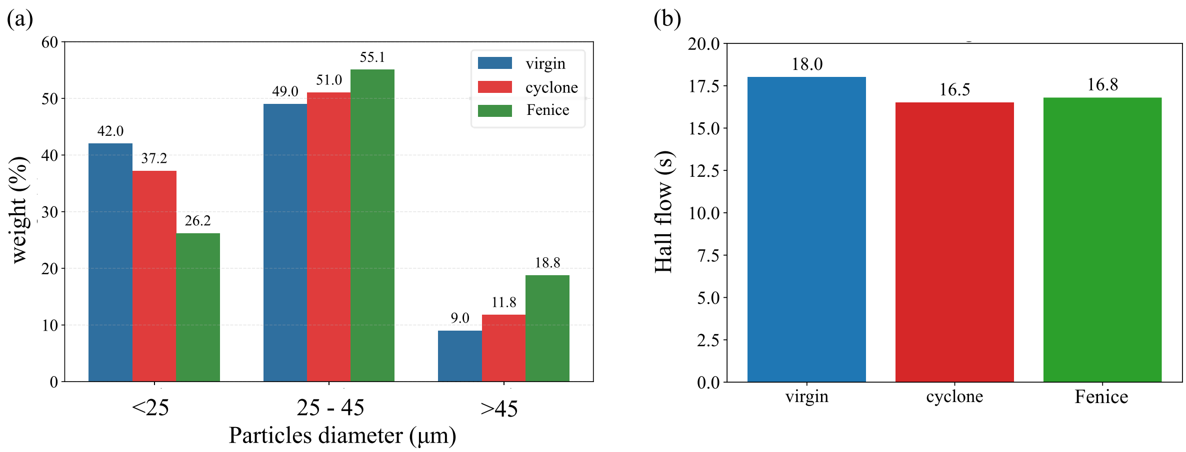

Fig. 2. (a) Comparison between PSD and (b) flowability of virgin [32], cyclone and Fenice powders.

1(a). Preliminary fatigue tests, performed with stress ratio, defined as the ratio between the minimum and the maximum imposed stress, equal to R = 0 indicated a marked reduction in fatigue performance when using 100% Fenice powder with respect to mixed powder and specimens manufactured from 100% virgin powder as reported in [20]. Accordingly, the adopted 50 wt% recycled content represents a deliberate compromise between enhanced sustainability and acceptable fatigue performance. More details about the experimental set-up behind fatigue tests will be provided below in the section dedicated to the description of mechanical tests. The chemical composition of the powder, reported in Table 1, was assessed by inductively coupled plasma optical emission spectroscopy (ICP-OES) in accordance with the ASTM E2594-20 standard. Carbon and oxygen contents were quantified using combustion-based methods, employing an oxygen atmosphere for carbon determination and an inert gas environment for oxygen analysis, following the ASTM E1019-18 standard. The oxygen content was found to be lower than 0.025%, thus in line with the threshold indicated by the ASTM F3055. The chemical composition of virgin powder was obtained by the authors in their previous research [32]. Table 2 shows that the ratios of Ti, Nb, Fe, Mo, Cr, and Al to Ni were slightly lower in the Fenice powder than in the cyclone and virgin powders, where they were nearly identical. Powder analyses were carried out using a scanning electron microscope (SEM- Jeol IT 300), and all the three different types of powder had a spherical morphology with some satellites on the surface as shown in Fig. 1(b)-(d). The PSD, reported in Fig. 2(a) for virgin, cyclone and Fenice powders, was evaluated using sieve analysis on a 100 g batch, using two sieves (25 μm and 45 μm) since most of the particles were finer than 45 μm, and the results demonstrated that most of the particle diameters ranged from 25 μm to 45 μm for all the specimens. Powder flowability was also assessed using a Hall flowmeter funnel following the ASTM B213 standard. In this test, 50 g of powder flowed through a calibrated funnel with a standardized outlet, and the time for complete discharge was recorded. Each measurement was repeated three times for each powder condition (virgin, cyclone, and Fenice), and the obtained average values are reported in Fig. 2(b). The flow times obtained served as indicators of powder flowability, with shorter times indicating better flow behaviour. Results show that the cyclone powder exhibited slightly improved flowability compared to Fenice powder, likely due to its slightly better balance between fine and coarser particle-size fraction and more favourable particle morphology.

2.2. Specimens manufacturing

Three kinds of specimens, i.e. plain without notches, blunt V-notched with nominal notch radius equal to R_N = 1 mm (VR1) and severe V-notched specimen with a nominal notch radius equal to R_N = 0.3 mm (VR03), were manufactured. Their mechanical drawings are reported in Fig. 3. The main parameters for the LPBF process were the laser power P, the scan velocity v, the hatch distance h, the layer thickness t, the meltpool aspect ratio A_r, which was equal to the ratio between the length l and the diameter $2r$ of the pool both calculated according to [40,78], the energy density defined as $E_d = P/thv$ and the LPBF build ratio equal to $B_r = thv$. All the specimens were manufactured by using LPBF process parameters that had been previously employed for virgin Inconel 718 as described in [20,32,40]. According to the work of Moda et al. [78], the used parameters enabled to mostly avoid the presence of keyhole defects, lack of fusion and internal pores. A stripe scanning approach was implemented for the hatching area rotating each layer by 67°. The specimens were manufactured through the above mentioned Renishaw RenAM 500S Flex LPBF machine installed at the metal AM laboratory of the University of Pisa and in single batches to avoid possible differences among the specimens of the same powder batch. In addition, the build platform was pre-heated at 170 °C to reduce residual stresses and

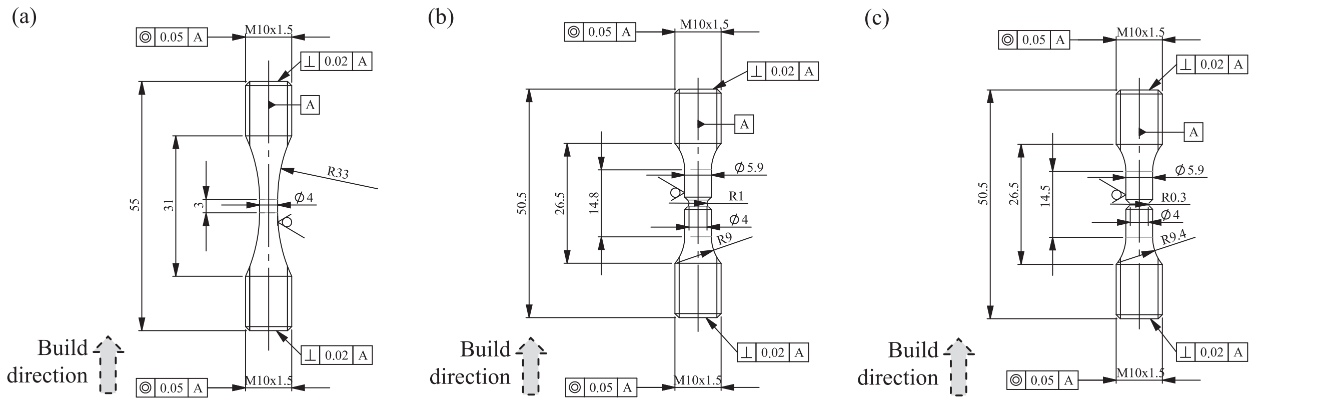

Fig. 3. Technical drawings, after machining of the threaded ends, of: (a) plain specimen, (b) VR1 specimen and (c) VR03 specimen. The dimensions are in mm.

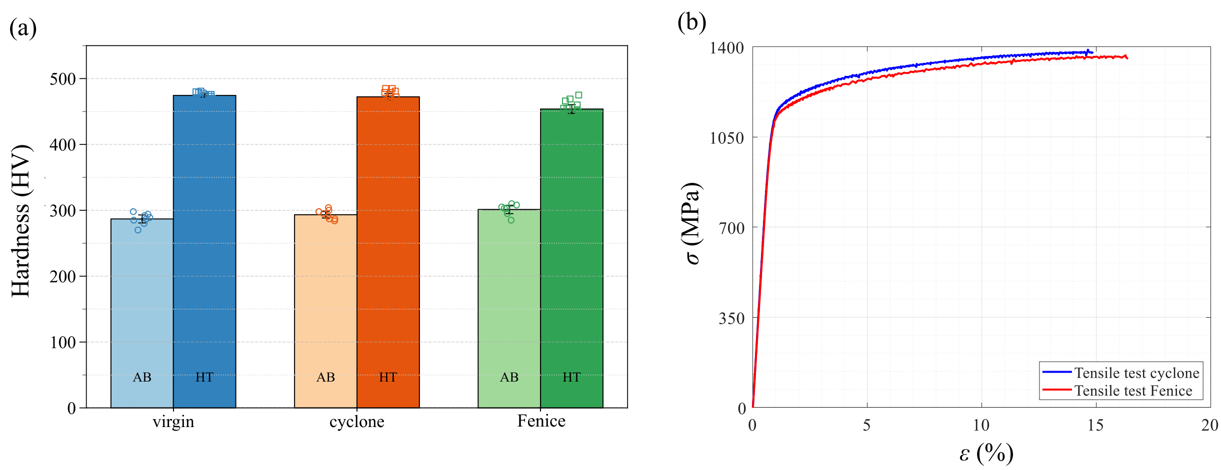

Fig. 4. Results of (a) hardness measurements for virgin [32], cyclone and Fenice specimens and (b) tensile tests on cyclone and Fenice specimens.

the printing chamber was filled of Argon gas to obtain an oxygen concentration lower than 7 parts per million by weight. In order to enhance the hardness of the manufactured specimens, these latter underwent an aging treatment, consisting of a first solution treatment phase followed by a double aging phase. This latter was coherent with the works of Zhang et al. in [79] and Macoretta et al. [20].

2.3. Mechanical tests results

2.3.1. Static mechanical tests

Vickers microhardness tests were carried out on mounted samples using a microhardness tester (FM-310, Future-Tech Corp.). An applied load of 50 g (HV0.05) was used for the measurements. On each sample, ten indentations were performed, and the mean hardness value HV_{av} along with the standard deviation σ_{HV} were determined, and they are shown in Fig. 4(a) for virgin [32], cyclone and Fenice specimens in AB and heat-treated (HT) conditions. As expected, due to formation of precipitates, the HV values of the HT specimens were higher than the corresponding ones of AB specimens. In particular, the average Vickers hardness value of AB specimens was equal to $HV_{av} = 293$, while the detailed obtained values of HV_{av} and standard deviation σ_{HV} for HT specimens are reported in Table 3 where it is worth noting that the obtained $HV_{av,F}$ of Fenice specimens was approximately 7% lower than the corresponding one obtained from virgin specimens $HV_{av,v}$, while $HV_{av,c}$ value of HT cyclone was aligned with $HV_{av,v}$. According to ASTM E8-16 standard, cylindrical dog-bone specimens having a gauge diameter of 4 mm were used for tensile tests. Monotonic tensile tests (initial strain rate of 1×10^{-4} s^{-1}) were performed at room temperature using a servo-hydraulic universal testing machine INSTRON 1343 equipped with hydraulic grips, a load cell of 100 kN and an axial extensometer (10 mm gauge length). Five tests were replicated for each experimental condition. The results of two exemplary tensile tests for cyclone and Fenice specimens are shown in Fig. 4(b). The main static properties, such as the Young modulus E, the yield strength S_Y, the ultimate strength S_U, the area reduction AR and the elongation at fracture eR are reported in Table 4. From the obtained results it can be noted that Fenice specimens showed slightly lower S_U value than cyclone specimens, while AR and eR values of Fenice specimens were slightly higher than the corresponding ones of cyclone specimens.

2.3.2. Fatigue tests

Finally, fatigue tests were carried out at room temperature with a RUMUL Mikrotron resonant testing machine equipped with a 20 kN load cell, with a testing frequency around 100 Hz, and the imposed stress ratio was equal to R = 0. Basquin's power law was used to describe the dependence between the stress amplitude and the number of cycles to failure as reported in Eq. (1a). The standard deviation σ_f was also calculated according to Eq. (1b) where $\sigma_{a,i}$ and $\hat{\sigma}_{a,i}$ indicate the experimental stress amplitude and the predicted stress amplitude through Basquin equation, respectively, while N and q represent the number of experimental data and the number of parameters of the used fitting curve, respectively. The obtained data with the fitted Basquin's law and curves at 10% and 90% of probability are shown in Fig. 5. The main results of fatigue tests are reported in Table 5. From the results of Fig. 5 and Table 5 it can be noted that Fenice specimens constantly showed slightly lower fatigue strength values than cyclone specimens.

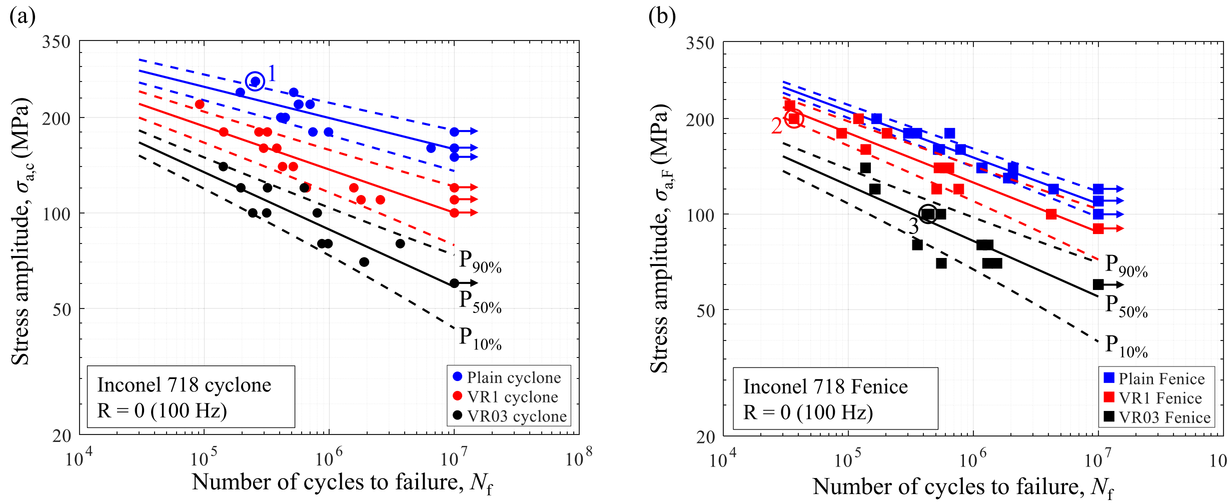

Fig. 5. SN curves of plain and V-notched specimens (a) cyclone and (b) Fenice.

Table 3
Mean and standard deviation hardness values measured on the HT specimens manufactured through virgin [32], cyclone and Fenice powders.

Specimen type	HV_{av} (HT)	σ_{HV} (HT)
Virgin	482	10.2
Cyclone	472	8.74
Fenice	453	12.2

2.3.3. Explanation of mechanical test results

In the end, the mechanical tests demonstrated that HT Fenice specimens had slightly lower ultimate strength, fatigue strength and hardness than HT cyclone specimens, while HT Fenice specimens exhibited slightly higher ductility than HT cyclone specimens. The obtained findings can be firstly explained considering that, as shown in Table 2, Fenice powder had lower ratios of Fe, Cr, Mo, Nb, Ti and Al to Ni than cyclone powder. Higher ratios of Fe, Mo, and Cr to Ni contribute to the strengthening of the γ-Ni matrix through solid-solution hardening, while lower ratios of Ti, Nb and Al to Ni lead to a slightly reduced/shifted γ'' and γ' precipitation thus reducing hardness and, as a consequence, ultimate and fatigue strength. Other minor influencing factors were represented by the combined effects of PSD and flowability. In fact, cyclone powder exhibited a slightly better balance between small and big particles, which contributed to improve flowability thus resulting in enhancing powder spreading during LPBF process and contributing to slightly increase the static and fatigue strength values.

$$\sigma_a = k N_f^b \tag{1a}$$

$$\sigma_f = \sqrt{\frac{\sum_{i=1}^{N} \left(\sigma_{a,i} - \hat{\sigma}_{a,i}\right)^2}{N - q}} \tag{1b}$$

2.4. Fractographic, microstructural and surface analyses

Fractographic analyses were performed through SEM, and explanatory examples of the obtained results for plain, VR1 and VR03 specimens are reported in Fig. 6(a)–(c) with the corresponding amplitude loading values, which correspond to points 1, 2 and 3 in Fig. 5. In Fig. 6(a)–(c), it is worth noting that fatigue failure was mostly due to a combination of detrimental effects provided by the pores and the surface roughness. Crack initiation sites were investigated as reported in Table 6 showing that fatigue crack always started from roughness valleys thus demonstrating that surface roughness always acted as predominant stress concentrator. Given the contribution of pores in enhancing the stress concentration at roughness valleys, unetched metallographic sections were specifically prepared to enable the morphological characterization, and some examples are shown in Fig. 6(d). Firstly, the shape factor of the pores was investigated through the software ImageJ and Eq. (2) where *Area* and *P* represent the area and the perimeter of the defect, respectively. The mean values of f_s obtained for cyclone and Fenice specimens were equal to $f_s = 0.973$ and $f_s = 0.984$, respectively. The obtained values of f_s were very close to one, thus suggesting almost spherical shape, which is coherent with pores originated from entrapped gas bubbles rather than lack of fusion or keyhole defects. The statistical analysis of pore diameters and locations was implemented according to [80], which was inspired by ASTM E2283, thus by using at least 24 cross-sections with 4 cross-sections extracted from 6 different specimens. From each cross-section the maximum pore diameter *D*, according to block maxima approach, and the corresponding distance from external surface *d* were extracted. Finally, the average of maximum pore diameters obtained from each kind of specimen was multiplied by the area of the cross section, thus obtaining the reference volume V_0 according to Murakami approach [35], which represented a quantification of the scanned volumes for each kind of specimen.

$$f_S = \frac{4\pi Area}{P^2} \tag{2}$$

The precipitates of cyclone and Fenice specimens were analysed through SEM, and three types of precipitates were recognized: δ-Ni3Nb mainly at the grain boundaries, very fine cubic γ'-Ni3Al and Ni3Ti coherently dispersed within the grains and fine plate-like γ''-Ni3Nb, coherently dispersed within the grains. A qualitative comparison indicated that the cyclone specimens exhibited a slightly finer and denser precipitate morphology, whereas Fenice specimens showed a more uniform and marginally coarser distribution. Overall, SEM observations suggested subtle differences in precipitate morphology between the cyclone and Fenice specimens, although the precipitation microstructure remained broadly comparable. The obtained results in terms of microstructure are presented in Fig. 7, and they were coherent with the corresponding ones obtained, for Inconel 718 virgin powder, in [32,81–85].

A 2D profilometer was used to reconstruct the surface topography of the specimens. The surface profiles were extracted from the regions of interest for the structural integrity assessment of the manufactured specimens, i.e. the zone with constant diameter and the notch region of the plain and V-notched specimens, respectively, as shown in Fig. 8(a). Once extracted, the profiles were used to calculate the reference surface S_0, according to [35] and as shown in Fig. 8(b), as $S_0 = L_0 h_p$, i.e. by multiplying the sampling length of the profile L_0 and h_p, which was

Table 4
Main static properties obtained for cyclone and Fenice specimens.

Specimen type	E GPa	S_Y MPa	S_U MPa	AR %	eR %
Cyclone (HT)	147.5 ± 0.5	1127 ± 8	1391 ± 2	17.2 ± 1.5	15.6 ± 0.8
Fenice (HT)	144.9 ± 1.6	1120 ± 5	1327 ± 12	21.4 ± 1.8	17.4 ± 1.5

Table 5
Numerical values obtained from the fitting operation on the experimental fatigue data.

Specimen type	Fitted Basquin law	Exp. Fatigue limit (10^7 cycles) MPa	σ_f MPa
Plain cyclone	$k = 774$ MPa, $b = -9.83 \times 10^{-2}$	159	18.2
VR1 cyclone	$k = 899$ MPa, $b = -0.136$	100	16.4
VR03 cyclone	$k = 1.07 \times 10^3$ MPa, $b = -0.181$	58.5	11.9
Plain Fenice	$k = 1.13 \times 10^3$ MPa, $b = -0.146$	108	7.84
VR1 Fenice	$k = 1.09 \times 10^3$ MPa, $b = -0.156$	87.8	12.4
VR03 Fenice	$k = 928$ MPa, $b = -0.175$	55.0	12.0

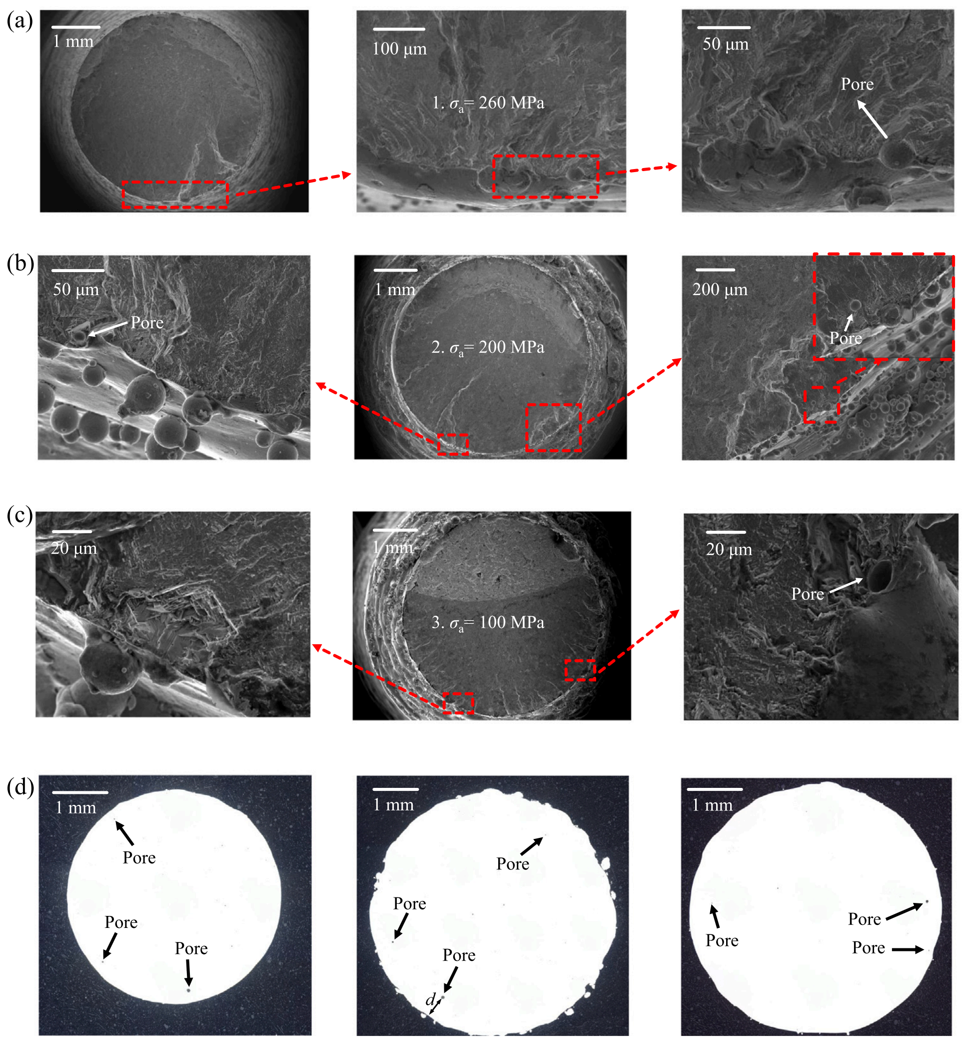

Fig. 6. Representative fractographic analyses of (a) cyclone plain specimen, (b) Fenice VR1 specimen, and (c) Fenice VR03 specimen, together with (d) explanatory OM analyses for the plain, VR1, and VR03 specimens.

equal to the distance between the mean profile and the deepest valley. Since multiple scans were performed for each type of specimen, the resulting S_0 values were averaged to obtain a representative reference surface for each specimen type. An example of a roughness profile is reported in Fig. 8(c), and the value of h_p is indicated. The obtained values of V_0 and S_0 for cyclone and Fenice specimens are reported in Table 7 where it is worth noting that the values of S_0 of the V-notched specimens are higher than the corresponding ones of the plain specimens, and S_0 values of VR03 specimens are higher than those of VR1 specimens. These latter results can be motivated considering that, during AM processes, V-notched specimens tend to have lower surface quality than plain specimens in the downskin region, especially for an

Table 6
Crack initiation sites.

Specimen	Initiations at surface	Initiations at internal pore	Initiations at near-surface pore
Plain cyclone	12/12	0/12	0/12
VR1 cyclone	12/12	0/12	0/12
VR03 cyclone	11/11	0/11	0/11
Plain Fenice	11/11	0/11	0/11
VR1 Fenice	12/12	0/12	0/12
VR03 Fenice	12/12	0/12	0/12

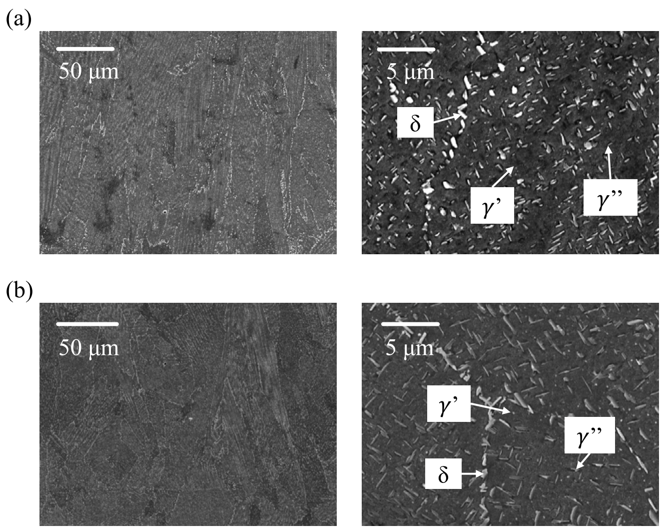

Fig. 7. Microstructural analysis of HT (a) cyclone and (b) Fenice specimens.

increasing severity of the notch, as already shown by Macoretta et a. in [20].

2.5. Statistical analysis of pores

Spearman r_S and Kendall r_K correlation factors were used to investigate the possible correlation between D and d for the various types of specimens, and the corresponding expressions are reported in Eq. (3). In Spearman correlation factor, $\mathrm{R}[x]$ and $\mathrm{R}[y]$ indicate the ranks of the random variables x and y. Low correlation factors were obtained between the two quantities, such as $|r_S, r_K| \ll 0.4$, by using both methods. Even if, according to [86], low correlation factors did not exclude a possible relationship between the two variables, D and d were analysed separately during the research. The cumulative distribution was calculated as $F = i/(N+1)$ as recommended by Murakami in [35]. According to [35] and for the sake of generalization, the generalized extreme value (GEV) distribution, reported in Eq. (4a), was used to analyse the distributions of D. The identification of the parameters was performed through nonlinear regression, and low significance values were obtained for parameter ζ in plain specimens, thus in this case the number of parameters of the distribution was reduced to 2, and the EVS, i.e. Gumbel distribution described in Eq. (4b), was used. In addition, the Kolmogorov–Smirnov hypothesis test was used, the corresponding p-values for D distributions are reported in Table 8, and their high values surely enhanced the use of the chosen distributions in describing the experimental data. As concerns d distributions, the authors obtained high p-values, reported in Table 9, through the exponential distribution described in Eq. (4c), and this result is coherent with that of [32]. The identified parameters of the used distributions, with the corresponding confidence intervals at 80%, are shown in Table 9, while example of experimental data for each kind of geometry with the corresponding fitted distributions are reported in Fig. 9.

$$r_s = \frac{\mathrm{cov}\left(\mathrm{R}[x], \mathrm{R}[y]\right)}{\sigma_{\mathrm{R}[x]}\sigma_{\mathrm{R}[y]}} \tag{3a}$$

$$r_k = \frac{2}{n(n-1)} \sum_{i=1}^{n-1} \sum_{j=i+1}^{n} \mathrm{sgn}\left(x_i - x_j\right) \mathrm{sgn}\left(y_i - y_j\right) \tag{3b}$$

$$F_V = \exp\left[-\left(1 + \zeta \frac{D - \mu_{\mathrm{gev}}}{\sigma_{\mathrm{gev}}}\right)^{-\frac{1}{\zeta}}\right] \tag{4a}$$

$$F_G = \exp\left[-\exp\left(-\frac{D-b}{a}\right)\right] \tag{4b}$$

$$F_E = 1 - \exp\left(-\frac{d}{\mu}\right) \tag{4c}$$

3. Fatigue strength modelling

3.1. FE simulations

FE simulations of pores and surface roughness, by using the elastic mechanical properties of Table 4 to define the material, were implemented to calculate the FSCFs. 2D axisymmetric FE models, with the submodelling technique, were implemented using the surface profiles obtained through the profilometer, and an example is shown in Fig. 10(a) for a plain specimen. Given the considered elastic behaviour of the material, unitary stress was considered in FE simulations. In the plain specimens, unitary stress was applied to the top surface as shown in Fig. 10(a), while in the V-notched specimens the stress applied to the top surface was equal to $\left(d_N/D_G\right)^2$, thus equal to the squared ratio between net and gross diameters, which were equal to 4 and 5.9 mm, respectively, as shown in Fig. 3(b) and (c). This approach enabled us to obtain unitary stress in the net section. Once the solution was obtained, the axial stress σ_x was extracted along radial paths originating from the nodes on the external surface where stress concentrations occurred. Since the FSCF is a dimensionless quantity, it was evaluated as the ratio between the average integral of the extracted σ_x, according to LM, and the unit stress σ_u as shown in Eq. (5a). This latter calculation was coherent with the fact that a unitary stress was considered in FE simulations. In addition, according to the work of Susmel and Taylor [87], the dependence of L on N_f was described through a power law as reported in Eq. (5b). In this work, TCD was not recalibrated, while, to enhance the robustness of the approach, coefficients A and B of Eq. (5b) were retrieved from previous research of the authors on virgin Inconel 718 [32], and they were equal to A = 24.0 µm and $B = -3.90 \times 10^{-2}$.

$$K_{f,\mathrm{rough}} = \frac{1}{2L\sigma_u} \int_0^{2L} \sigma_x \, \mathrm{d}y \tag{5a}$$

$$L = A\left(N_f\right)^B \tag{5b}$$

3D FE models were, instead, implemented to assess the FSCFs provided by the pores, and an example is shown in Fig. 10(b) for a VR1 specimen. Similarly to the 2D FE simulations, unitary stress was applied to the top surface of the plain specimen, while a stress value equal to $\left(d_N/D_G\right)^2$ was applied to the top surface of V-notched specimens. Given that the distances between the pores were much higher than L values as qualitatively shown in Fig. 6(d), a model with only one pore was deployed. Considering that, even in 3D FE simulations, a unitary stress was considered in the region of interest, once the models were solved, the FSCFs of pores in plain specimens were calculated by applying Eq. (5a) to radial paths extracted from nodes on the pore surfaces experiencing stress concentration. For each simulation, the radial path yielding the highest FSCF was selected for the analysis. On the contrary, the calculation of FSCFs provided by pores in V-notched specimens was not straightforward. In fact, three effects provided a key impact on the fatigue strength of V-notched components, i.e. the notch, the surface roughness and the pores. In principle, 3D FE simulations containing all the above mentioned features could be implemented, but they would require very high computational cost. To overcome this

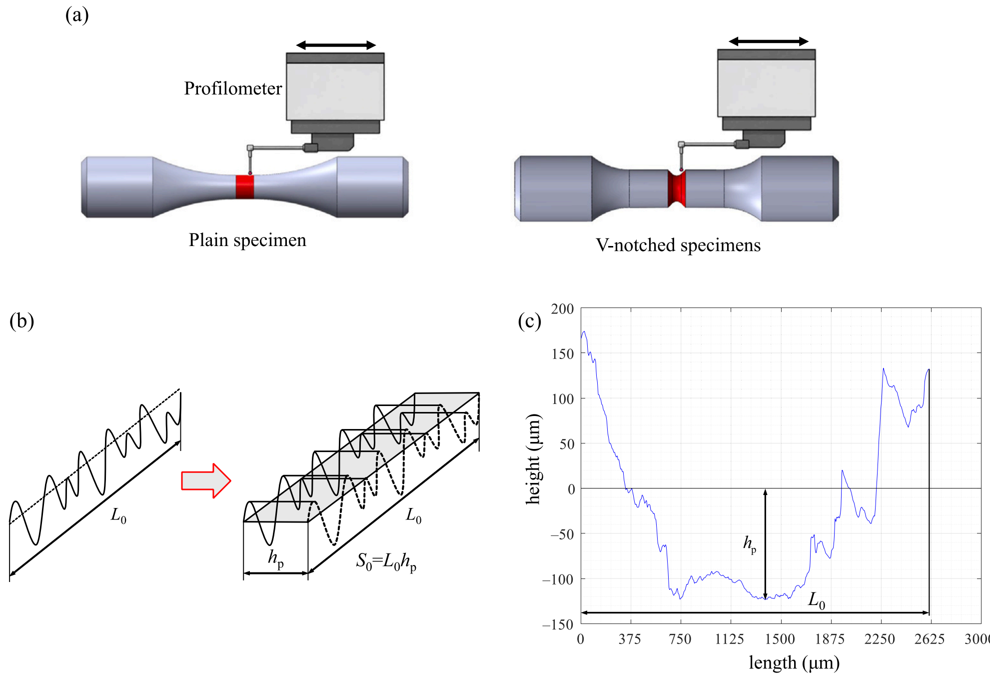

Fig. 8. (a) Explanatory figure to describe the extraction of surface profiles from plain and V-notched specimens, (b) Murakami model to obtain reference surface S_0 from one-dimensional roughness measurements and (c) example of h_p and L_0 obtained from a surface profile of the manufactured specimens.

Table 7
Values of the reference volumes and surfaces for the plain, VR1 and VR03 specimens manufactured both through cyclone and Fenice powders.

Specimen	Plain cyclone	VR1 cyclone	VR03 cyclone	Plain Fenice	VR1 Fenice	VR03 Fenice
V_0 (mm^3)	0.5105	0.5711	0.5990	0.4055	0.5550	0.4835
S_0 (mm^2)	0.1706	0.3960	0.8000	0.1776	0.3795	0.8672

Table 8
Obtained p-values for the considered probability distributions regarding pore diameters and distances from external surface of cyclone and Fenice specimens.

Specimen	Diameter (p-value)	Distance (p-value)
Plain cyclone	EVS: 0.954	Exponential: 0.944
VR1 cyclone	GEV: 0.919	Exponential: 0.857
VR03 cyclone	GEV: 0.997	Exponential: 0.944
Plain Fenice	EVS: 0.976	Exponential: 0.767
VR1 Fenice	GEV: 0.964	Exponential: 0.866
VR03 Fenice	GEV: 0.979	Exponential: 0.891

issue, 2D axisymmetric FE simulations, with surface roughness and the notch as described above, and 3D FE simulations with the pore and the notch were implemented. However, this approach may result in double counting the notch effect given that it was included in both simulations. As a consequence, the FSCFs provided by the notch had to compensated in FE simulations of surface roughness or in those related to the pores. To achieve this, 2D axisymmetric FE simulations of the only notch were performed, and the axial stress $\sigma_{x,\mathrm{V}}$ was extracted on the notch bisector, and an example for the VR03 specimen is indicated by the blue line in Fig. 10(c). From the results of 3D FE simulations with the notch and the pore, two points were considered of interest for FSCF calculation, i.e. point A at notch apex and point B at pore apex as shown in Fig. 10(c), and the corresponding stress path for a VR03 specimen is indicated by the red curve in Fig. 10(c). The FSCFs provided by the only notch $K_{\mathrm{f,V,A}}$ and $K_{\mathrm{f,V,B}}$ were calculated starting from the above mentioned points through LM, i.e. the expressions presented in the first equation of Eq. (6). Finally, values of $K_{\mathrm{f,V,pore,A}}$ and $K_{\mathrm{f,V,pore,B}}$ were calculated through the second and third expressions of Eq. (6), i.e. by calculating the average integrals of $\sigma_{x,\mathrm{V,pore}}$, extracted from 3D FE simulations with the pore and the notch, starting from points A and B according to LM and by dividing the obtained result by the previously obtained values of $K_{\mathrm{f,V,A}}$ and $K_{\mathrm{f,V,B}}$. In conclusions, the proposed framework enabled to avoid double counting of notch effect, and the higher of the two values was identified as the FSCF.

$$\begin{cases} K_{\mathrm{f,V,A}} = \frac{1}{2L\sigma_{\mathrm{u}}}\int_{y_A}^{y_A+2L}\sigma_{x,\mathrm{V}}\,\mathrm{d}y \quad K_{\mathrm{f,V,B}} = \frac{1}{2L\sigma_{\mathrm{u}}}\int_{y_B-2L}^{y_B}\sigma_{x,\mathrm{V}}\,\mathrm{d}y \\ K_{\mathrm{f,V,pore,A}} = \frac{1}{2L\sigma_{\mathrm{u}}K_{\mathrm{f,V,A}}}\int_{y_A}^{y_A+2L}\sigma_{x,\mathrm{V,pore}}\,\mathrm{d}y \\ K_{\mathrm{f,V,pore,B}} = \frac{1}{2L\sigma_{\mathrm{u}}K_{\mathrm{f,V,B}}}\int_{y_B-2L}^{y_B}\sigma_{x,\mathrm{V,pore}}\,\mathrm{d}y \end{cases} \tag{6}$$

3.2. Nonlinear regression surrogate to assess the K_{f} of pores

3D FE simulations of pores required a high computational cost, thus performing the statistical analysis of a large dataset of FSCFs obtained from FE models became challenging and time-consuming. Considering the promising ability of nonlinear regression surrogate models [88], a feedforward ANN was designed and trained to describe the relationship between pore FSCFs (output) and the inputs D, d and L, thus enabling a robust assessment of FSCFs at high percentiles through a created synthetic population of pores. In addition, the authors added a flag as fourth input, which was equal to 0 for plain specimens and to 1 for V-notched specimens, and the fifth input corresponded to the nominal notch radius of the V-notched specimens. This latter variable was set equal to 0 for the plain specimens. The dataset was created by using the results of the FE simulations of the pores as described in 3.1 and the sizes of the input and output data matrices were equal to 5 × 5940 and 1 × 5940. The dataset of D, d and L to be used in FE simulations described in 3.1 was generated to enhance generalization ability of the

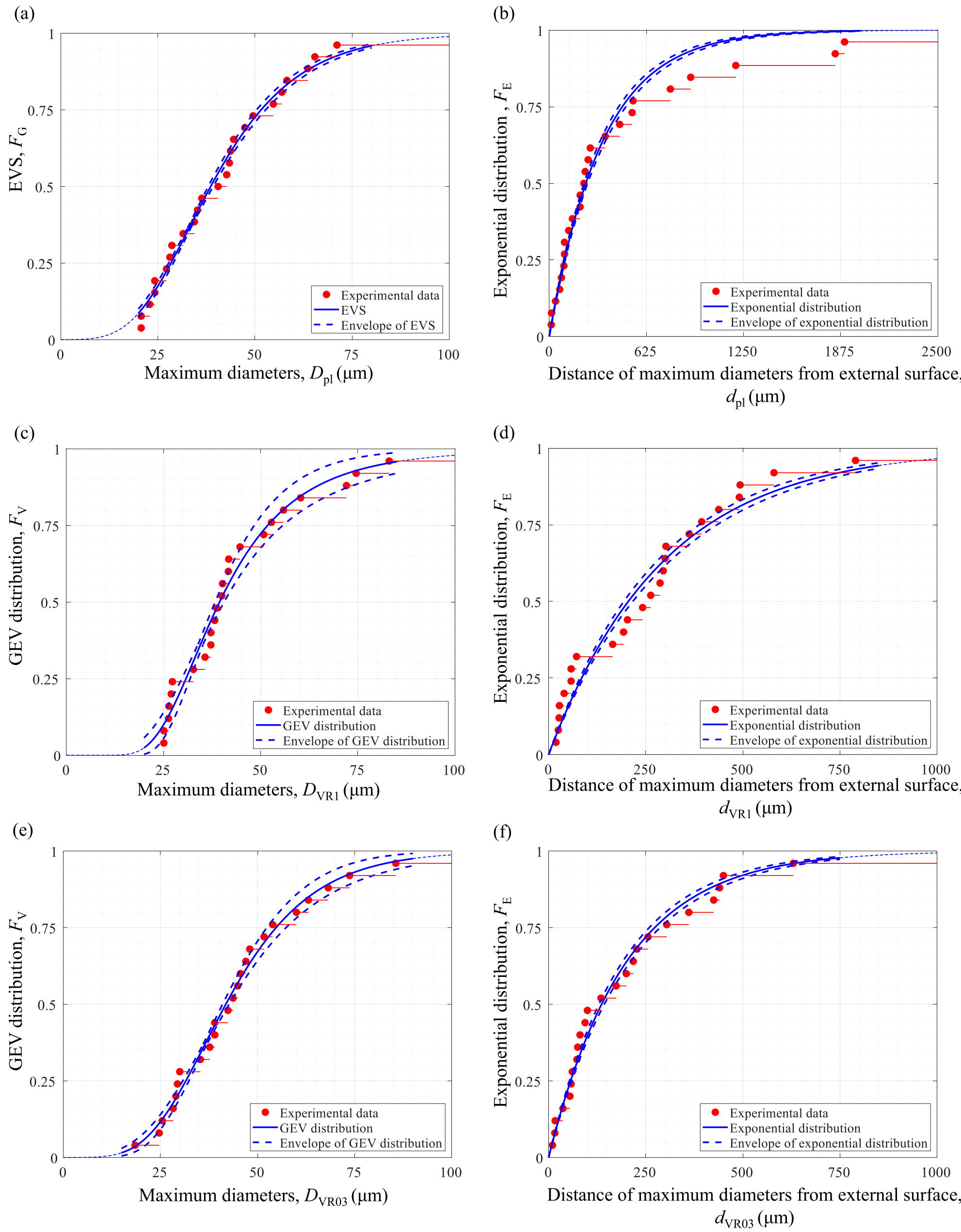

Fig. 9. Example of statistical analysis of pore diameters and locations in cyclone specimens: (a) EVS and (b) exponential distributions to model pore diameters and distances from external surface, respectively, in plain specimens and GEV and exponential distributions to model (c) pore diameters and (d) distances from external surface in VR1 specimens and (e) pore diameters and (f) distances from external surface in VR03 specimens.

CSM and to avoid extrapolations. Therefore, the sampled ranges were chosen to be significantly wider than the expected experimental ones. In particular, D values were sampled uniformly over the range extending from 0 to 50% above the value corresponding to the 99th percentile of the probability distributions reported in Table 9. A similar reasoning was implemented for d, and they were uniformly sampled within the range extending from the 1st percentile of probability distributions shown in Table 9 and the radii of the different specimens. For the critical distances, firstly, extreme values were calculated by applying Eq. (5b) to 3×10^4 and 10^7 number of cycles to failure, which, according to Fig. 5, corresponded to boundaries of the range of interest for the current research. Subsequently, L values were obtained by uniformly sampling between 10% of the lower bound and 110% of the upper bound.

The dataset was divided in the following way: 70% of the data was used for training, 15% for validation and the remaining 15% for independent testing, the hyperbolic tangent was used as activation function, while the MSE, reported in Eq. (7), between target y_i and estimated data $\hat{y}_i$ was used as loss function. According to the universal approximation theorem and to the expected continuous relationship between inputs and outputs, only one hidden layer of neurons was used. According to [88], the validation data enabled to identify the adequate number of hyperparameters of the ANN, and the number of neurons in the hidden layer was tuned by balancing between the MSE of the validation data and the training time, and the obtained results are reported in Table 10 for different number of neurons. The optimal condition was obtained by using 10 neurons in the hidden layer. The obtained results of MSE and R^2 for the denormalized data are presented in Fig. 11(a)–(d), while the MSE of the normalized data, by varying the number of epochs, is shown in Fig. 11(e). In order to evaluate the model generalization ability, the k-fold cross validation algorithm was implemented considering $k = 10$ folds. The algorithm

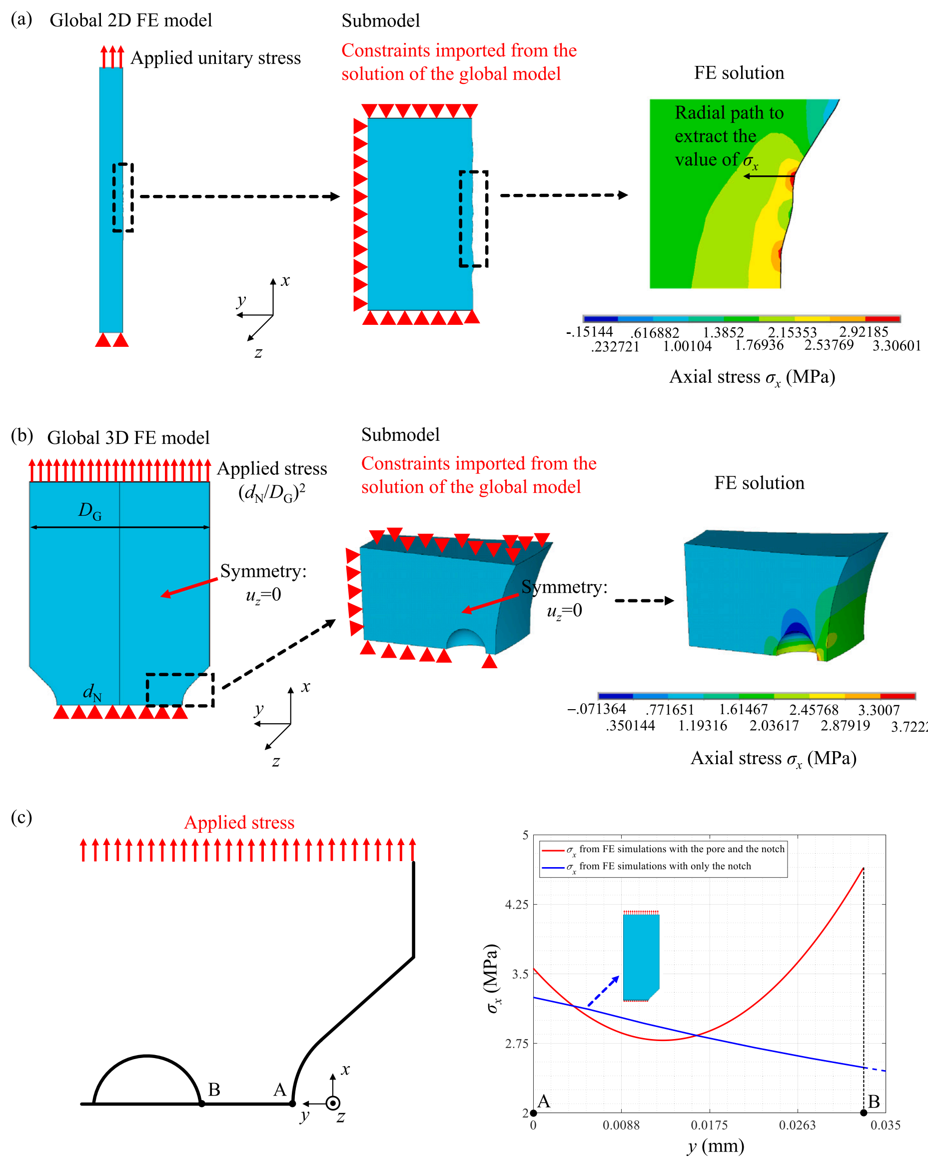

Fig. 10. Examples of (a) 2D FE model, with corresponding axial stress σ_x results, of a plain specimens with surface roughness, (b) 3D FE simulations, with corresponding axial stress σ_x results, of pores in VR1 specimens and (c) example of competition of stress raisers at pore and notch apexes and uniaxial stress distribution provided by the only notch.

consisted of using $k-1$ folds to train the model and the data of the remaining fold as test data, and the procedure was repeated 10 times, thus each fold was considered as test fold at least one time. The MSE and R^2 values obtained through the k-fold cross validation are reported in Fig. 12 for the test data, and their mean values were very similar to the corresponding ones presented in Fig. 11, thus confirming the generalization ability of the designed neural network regardless of the specific data split.

$$\mathcal{L} = \frac{1}{N}\sum_{i=1}^{N}\left(y_i - \hat{y}_i\right)^2 \tag{7}$$

An alternative CSM, providing physical constraints on the output values of pore FSCF, was also implemented, and the same architecture as that described above was used, while the loss function was modified to include physical constraints as reported in Eq. (8). In this latter, the first term is the classical MSE, while the second term represents a penalty to incorporate physical constraints into the loss function. The weight term λ was introduced to balance the aim of accurately fitting the target data and satisfying the physical constraints, and, given that the aim of the proposed CSM was to accurately reproduce pore FSCFs, the value of λ was set equal to 1 to balance the two purposes equally. Physical constraints were introduced in this second CSM, by penalizing output values of FSCFs outside the range provided by $K_{\mathrm{f,pore,min}}$ and $K_{\mathrm{f,pore,max}}$. In particular, the lower bound was imposed as $K_{\mathrm{f,pore,min}} = 1$ since the presence of pores cannot enhance the fatigue performance of a specimen. Therefore, a sample with a pore can only reach, at best, the same fatigue resistance as a pore-free specimen, but cannot exceed it. This limitation prevents any physically inconsistent improvement in fatigue strength attributable to the existence of pores. The upper bound was set equal to $K_{\mathrm{f,pore,max}} = 2$, based on multiple converging pieces of evidence. First, as clearly shown in Fig. 11(a)–(d), the predictions of the conventional ANN remained below 2 over the entire investigated domain. This result is particularly significant because the FE simulations used to generate the training dataset were deliberately performed over ranges of pore diameters, distances from the external surface, and critical distances substantially wider than those expected experimentally. Consequently, the ANN was trained on a conservative dataset covering input combinations well beyond the practical operating conditions,

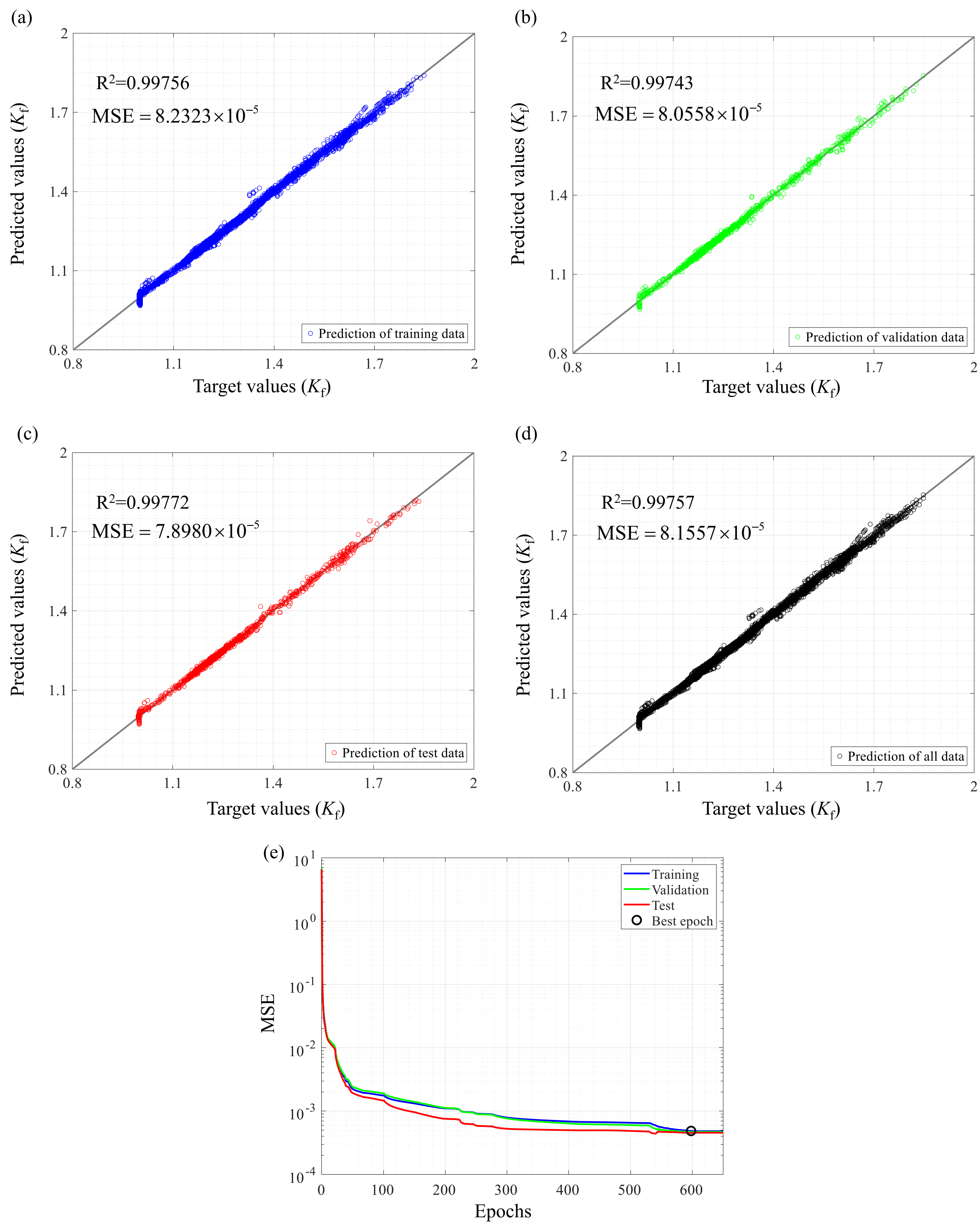

Fig. 11. Predictions of data-driven ANN for denormalized (a) training data, (b) validation data, (c) test data, (d) all data, (e) trend of MSE for normalized training, validation and test data during the training process by varying the number of epochs.

thereby enhancing its generalization capability while minimizing the need for extrapolation. Since the computed FSCF values never exceeded 2, even under these intentionally broad simulation conditions, selecting 2 as the upper bound represents a reasonable and physically justified choice. Finally, additional support for this value is provided by the literature: similar upper bound values of $K_{f,\mathrm{pore}}$ were reported in Ref. [89] for comparable pore diameters and distances from the external surface. The obtained results for this second type of CSM are reported in Fig. 13(a)–(d), where it is worth noting that the values of R^2 and MSE are lower and higher, respectively, than those of Fig. 11(a)–(d). This latter aspect can be explained considering the complexity of the loss function $\mathcal{L}'$ where additional nonlinear terms were introduced with respect to that of Eq. (7). Given the key role of FSCFs at 99th percentile, as better explained below, FSCFs of pores at 99th percentile were calculated through both CSMs and the comparison is shown in Fig. 13(e). In this latter figure, it is clearly highlighted that both architectures enabled us to obtain very similar values, and the obtained findings demonstrated that in this work, classical ANN can provide accurate results without compromising physics and with reasonable computational cost.

$$\mathcal{L}' = \frac{1}{N}\sum_{i=1}^{N}\left(y_i - \hat{y}_i\right)^2 + \frac{\lambda}{N}\sum_{i=1}^{N}\left[\max\left(0, \hat{y}_i - y_{i,\max}\right)^2 + \max\left(0, y_{i,\min} - \hat{y}_i\right)^2\right] \quad (8)$$

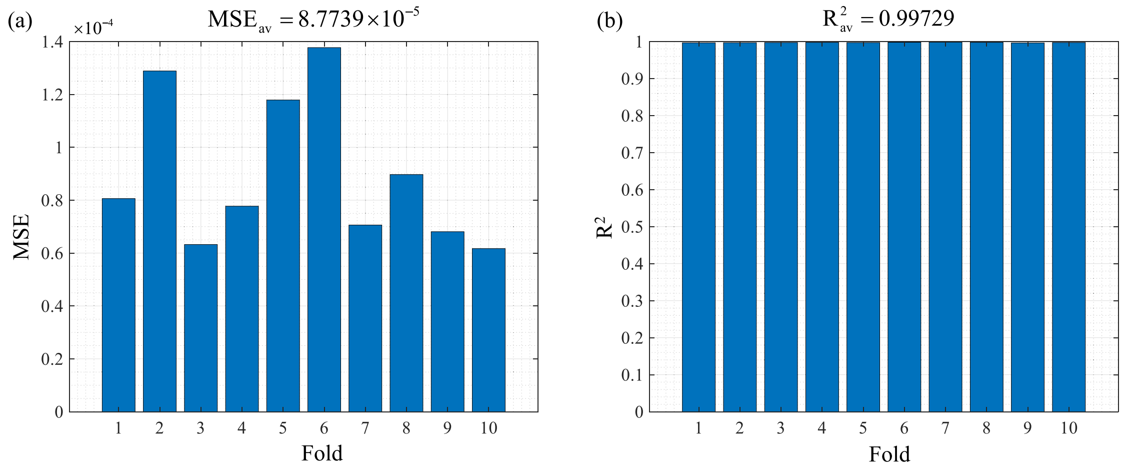

Fig. 12. Results of the k-fold cross validation for the denormalized test data in terms of (a) MSE and (b) R^2.

Table 9
Numerical values, with corresponding confidence intervals at 80%, obtained for the parameters of GEV, EVS and exponential distributions concerning pore diameters and distances from external surface of plain, VR1 and VR03 cyclone and Fenice specimens.

Quantity	Pore diameter	Distance from the external surface
Parameter 1 cyclone plain	$a = 14.7 \pm 0.6$ μm	$\mu = 339 \pm 17$ μm
Parameter 2 cyclone plain	$b = 33.2 \pm 0.4$ μm	/
Parameter 1 Fenice plain	$a = 8.73 \pm 0.66$ μm	$\mu = 81.9 \pm 4.7$ μm
Parameter 2 Fenice plain	$b = 25.5 \pm 0.4$ μm	/
Parameter 1 cyclone VR1	$\mu_{gev} = 34.7 \pm 0.6$ μm	$\mu = 290 \pm 16$ μm
Parameter 2 cyclone VR1	$\sigma_{gev} = 12.4 \pm 1.0$ μm	/
Parameter 3 cyclone VR1	$\zeta = 0.155 \pm 0.145$	/
Parameter 1 Fenice VR1	$\mu_{gev} = 33.5 \pm 0.5$ μm	$\mu = 238 \pm 12$ μm
Parameter 2 Fenice VR1	$\sigma_{gev} = 11.3 \pm 0.8$ μm	/
Parameter 3 Fenice VR1	$\zeta = 0.270 \pm 0.134$	/
Parameter 1 cyclone VR03	$\mu_{gev} = 36.4 \pm 0.5$ μm	$\mu = 196 \pm 7$ μm
Parameter 2 cyclone VR03	$\sigma_{gev} = 14.8 \pm 0.8$ μm	/
Parameter 3 cyclone VR03	$\zeta = -0.01 \pm 0.09$	/
Parameter 1 Fenice VR03	$\mu_{gev} = 28.9 \pm 0.3$ μm	$\mu = 215 \pm 10$ μm
Parameter 2 Fenice VR03	$\sigma_{gev} = 5.55 \pm 0.43$ μm	/
Parameter 3 Fenice VR03	$\zeta = 0.586 \pm 0.128$	/

The impact of the uncertainty of D, d and TCD values L on the output values of the ANN having the loss function defined by Eq. (7) was evaluated, and the uncertainty of D and d was modelled through the identified distribution functions presented in 2.5. On the other hand, the L values used in this research were retrieved from previous work of the authors [32], where they were calculated through the double notch approach [32] as in Eq. (9) where σ_a^* indicates the intrinsic fatigue strength, while the other quantities represent geometric or fatigue strength values of the two considered V-notched specimens. The fatigue strength values used in [32] to calculate L were retrieved, and it was considered that, for each N_f value, the distribution of the stress amplitude was a Gaussian having a mean value equal to that obtained from the corresponding fitted Basquin's curve and a standard deviation calculated through the residuals between experimental data and values predicted by the fitted Basquin's law. Eq. (9) was then solved considering 10 000 Gaussian values of stress amplitude for different N_f values and statistical uncertainty of TCD was evaluated. Finally, the dataset, composed of 10 000 L, D and d values, was used to calculate Borgonovo indices [90], as described by Eq. (10), by varying N_f. In this latter, N_{bin} indicates the number of bins in which the data were divided, while f_Y and $f_{Y|x_i \in bin_k}$ indicate the PDF of the output of the ANN and the PDF of the output of the ANN given fixed values of variable x_i belonging to bin_k, respectively. A high value of Borgonovo index indicates a high impact of the uncertainty of corresponding input value on the PDF of the output, and the implemented procedure is resumed in Fig. 14, while the obtained results are reported in Fig. 15. In this latter figure, it is worth noting that the uncertainty of L had the major impact on the output of the ANN, while the second major role was played by D in plain specimens and by d in V-notched specimen. The first obtained result can be explained considering a representative example reported in Fig. 16, where the high impact of TCD uncertainty on output FSCFS is quantitatively represented. The second major role played by d in V-notched specimens can be explained considering the competition between the stress fields starting from notch and pore apexes as shown in Fig. 10(c). Finally, in Fig. 15 the value of δ related to L shows an increasing trend as N_f increases. This latter result can be explained considering that the PDF of L was calculated considering constant values of the standard deviation by varying N_f thus for higher values of N_f the coefficient of variation of stress amplitude increased

Table 10
MSE of denormalized validation data and training times by varying the number of neurons of the hidden layer.

Number of neurons	MSE_{val}	Training time (s)
5	6.50×10^{-4}	1
10	8.06×10^{-5}	2
15	3.60×10^{-5}	9
20	8.00×10^{-5}	6

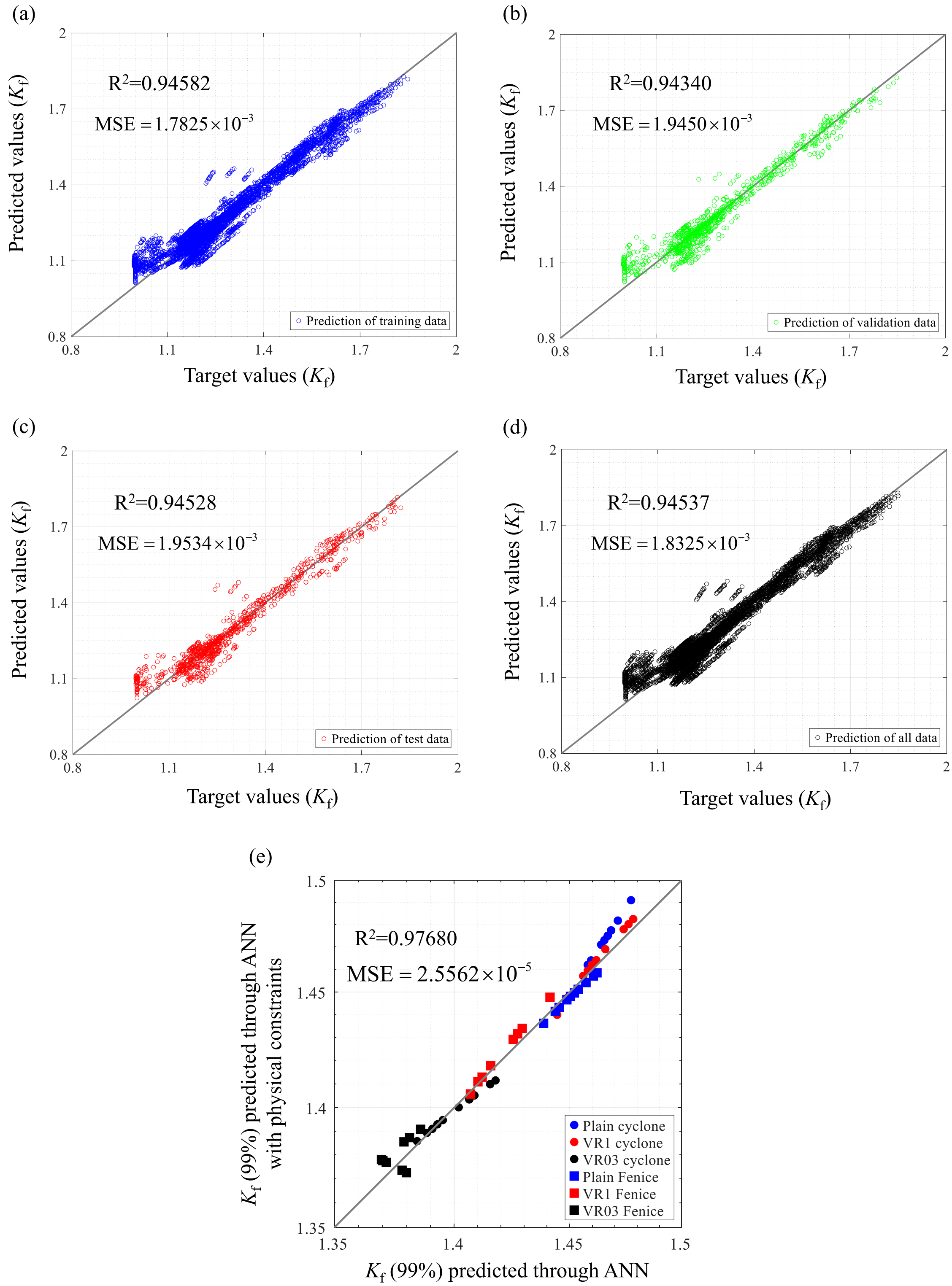

Fig. 13. Predictions of the neural network with modified loss function to incorporate physical constraints for denormalized (a) training data, (b) validation data, (c) test data, (d) all data and (e) comparison of the 99th percentile values of $K_{\mathrm{f,pore}}$ with those obtained using the ANN with MSE loss function.

indicating data dispersion growing relative to the mean value.

$$\begin{cases} \frac{D_{02}}{2}\, g\left(\frac{R_{02}}{D_{02}/2}, \frac{\sigma_a^*}{\sigma_{\mathrm{VR02,m,a}}}\right) = \frac{D_1}{2}\, g\left(\frac{R_1}{D_1/2}, \frac{\sigma_a^*}{\sigma_{\mathrm{VR1,m,a}}}\right) \\ L = \frac{D_{02}}{2}\, g\left(\frac{R_{02}}{D_{02}/2}, \frac{\sigma_a^*}{\sigma_{\mathrm{VR02,m,a}}}\right) \end{cases} \tag{9}$$

$$\delta_i = \frac{1}{2}\sum_{k=1}^{N_{\mathrm{bin}}}\left(\frac{n_k}{N}\right)\int_{-\infty}^{+\infty}\left|f_{\mathrm{Y}} - f_{\mathrm{Y}|x_i\in \mathrm{bin}_k}\right|\mathrm{d}x \tag{10}$$

3.3. Fatigue strength predictions and final discussion

The outcomes of FE simulations and the ANN with loss function described by Eq. (7) were used to calculate the predicted values of fatigue strength and number of cycles to failure. The FSCFs provided by pores and surface profiles were evaluated at 99th percentile, given its proved

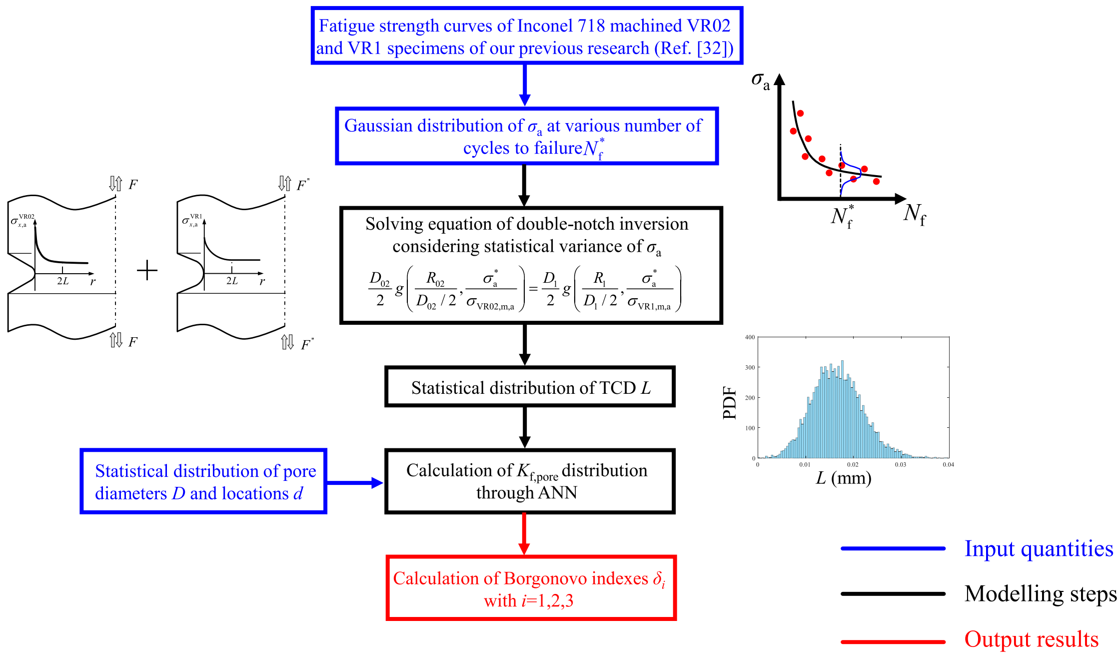

Fig. 14. Logic flow behind the calculation of Borgonovo indices.

ability in assessing the FSCF of flawed materials as described in [32,91], and also at 95th percentile for comparison. The FSCFs obtained from FE simulations of the surface profiles were fitted through EVS as shown in Fig. 17(a). However, according to the size effect, the modelled profiles did not entirely cover the highly-stressed regions, and this aspect has a key impact on fatigue strength assessment [92]. This latter aspect was firstly considered by calculating, from 2D FE simulations of plain and V-notched specimens, the highly-stressed surface (HSS) at 95% of the axial peak stress. This threshold proved to be an efficient indicator of HSS as demonstrated by Benedetti et al. in [93], and the obtained values were equal to HSS = 80.7, 3.51 and 0.837 mm^2 for the plain, the VR1 and the VR03 specimens, respectively. The value of the size ratio α was then calculated according to Eq. (11)(a), while Eq. (11)(b) was used to obtain the FSCFs at 95th and 99th percentiles in the HSS (X_P) considering the FSCFs in the reference surface ($X_{P,0}$) and the ratio between $F^{-1}\left(P^{1/\alpha}\right)$ and $F^{-1}(P)$ where F represented the EVS used to describe the FSCFs obtained from FE simulations and P was equal to $P = 0.95$ or $P = 0.99$ depending on the considered percentile. Eq. (11) was coherent with the proposal of Makkonen et al. [94].

$$\begin{aligned}
&\text{(a)} \begin{cases} \alpha = \frac{\text{HSS}}{S_0} & \text{if} \quad \text{HSS} > S_0 \\ \alpha = \frac{S_0}{\text{HSS}} & \text{if} \quad \text{HSS} < S_0 \end{cases} \\
&\text{(b)} \begin{cases} X_P = X_{P,0} \frac{F^{-1}(P^{1/\alpha})}{F^{-1}(P)} & \text{if} \quad \text{HSS} > S_0 \\ X_P = X_{P,0} / \left(\frac{F^{-1}(P^{1/\alpha})}{F^{-1}(P)}\right) & \text{if} \quad \text{HSS} < S_0 \end{cases}
\end{aligned} \tag{11}$$

To calculate the FSCFs provided by the pores, the highly stressed volumes (HSVs) at 95% of the maximum axial stress were calculated for the three specimens, and the obtained values were equal to HSV = 67.6, 5.55×10^{-2} and 3.40×10^{-3} mm^3 for the plain, VR1 and VR03 specimens, respectively. Like the HSSs, the HSVs were calculated through simple axisymmetric 2D FE simulations of the defect-free specimens. The size ratio α was then obtained through Eq. (11)(a) by using volumes instead of surfaces and through V_0 values presented in Table 7. The introduction of the size ratio was necessary to account for the differences between V_0 values, corresponding to the scanned regions according to Murakami model [35], and the HSVs. Afterwards, 100 000 values of P, ranged between 0 and 1, were generated from a uniform probability distribution, and the corresponding synthetic populations of 100 000 D and d values were obtained for each type of specimen using Eq. (11)(b). In Eq. (11)(b), $X_{P,0}$ indicates the values of D and d according to Eq. (4), while F indicates the cumulative distributions of Eq. (4). The generated synthetic populations of D and d were then substituted into the developed CSM presented in Section 3.2 together with L values. These latter were obtained, through Eq. (5b), at the number of cycles to failure corresponding to the experimental data presented in Fig. 5. It is worth noting that CSM and experimental data are employed at two distinct levels: the first to provide a deterministic relationship between pore FSCFs and D, d, L values and specimen type, while the second as input of the developed CSM for fatigue strength assessment of the manufactured specimens. Given the very high amount of data, the sampling distribution of pore FSCFs obtained from the ANN was directly used to identify the corresponding values at 95th and 99th percentiles as shown in Fig. 17(b). In addition, the differences between FSCFs of pores and surface roughness at 99th percentile for plain specimens made of cyclone and Fenice powders are reported in Fig. 17(c) and (d), and the FSCFs associated with surface roughness were always higher than those associated with pores confirming the experimental findings presented in Table 6. An explanatory comparison between stress profiles obtained through FE simulations of surface profiles and pores is presented in Fig. 17(e), where it is highlighted that, for L = 13.5 μm, the FSCF provided by surface roughness is higher than the corresponding value provided by the pore. Given that L and σ_a^* values of virgin specimens obtained in [32] were used in current research, the last degradation effect $K_{f,hard}$ was represented by the decrease of $HV_{av,c}$ and $HV_{av,F}$ with respect to hardness of virgin specimens $HV_{av,v}$ according to the Murakami approach [35]. The values of $K_{f,hard}$ were calculated through the ratio of HV values at the bottom of the confidence intervals as shown in Eq. (12a).

Finally, to provide a conservative and statistical assessment, the total FSCF $K_{f,tot}$ was calculated as presented in Eq. (12b), and all the procedure to calculate the predicted values of fatigue strength and number of cycles to failure, mainly based on Eq. (12c), is resumed in Fig. 18. The predicted values of fatigue strength and number of cycles to failure, through the use of FSCFs at 99th and 95th percentiles, are reported in Fig. 19. The differences between experimental and

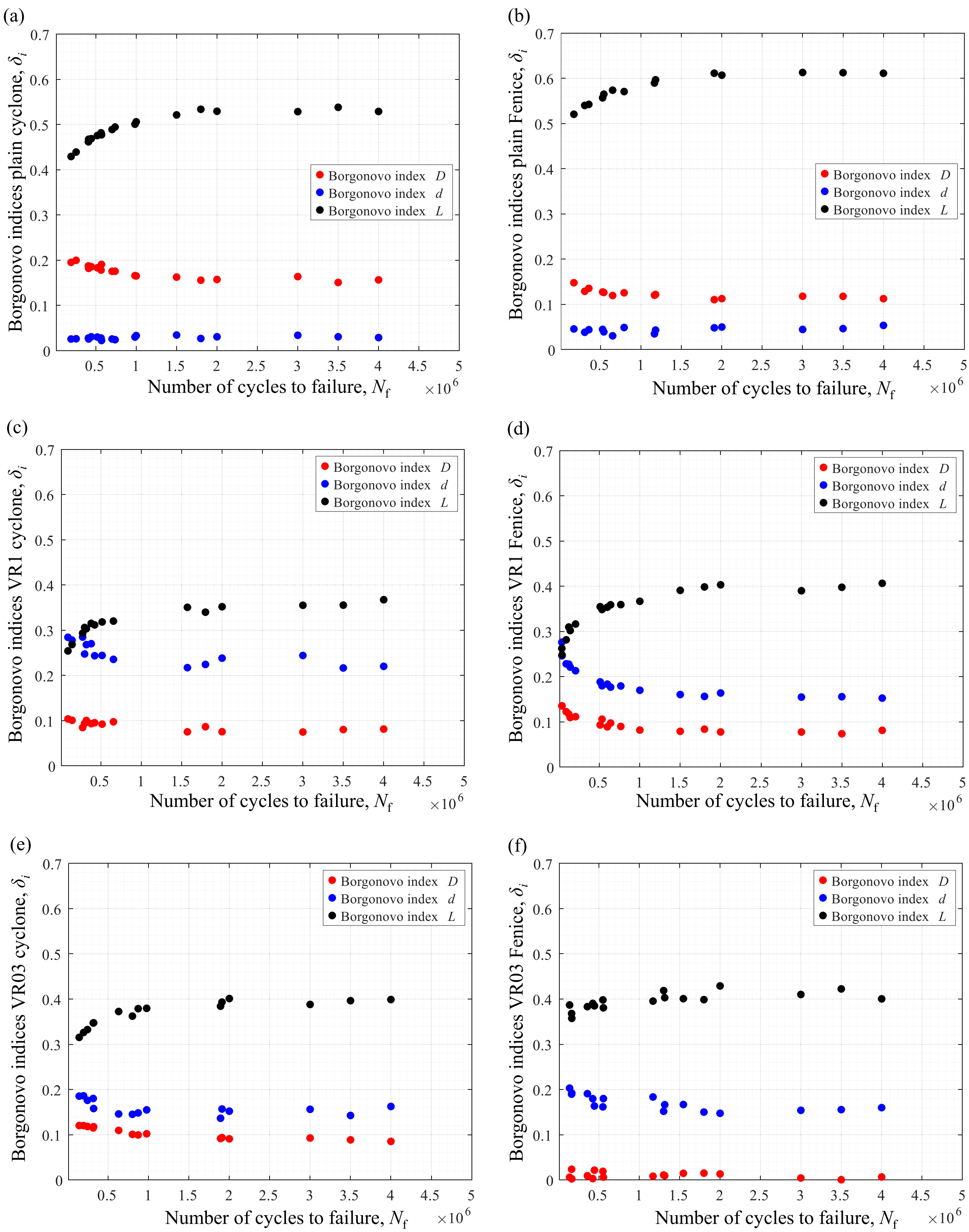

Fig. 15. Borgonovo indices for pore diameter D, pore distance from external surface d and critical distance L for (a) cyclone plain, (b) Fenice plain, (c) cyclone VR1, (d) Fenice VR1, (e) cyclone VR03 and (e) Fenice VR03.

predicted N_f values was assessed through the symmetric mean absolute percentage error (SMAPE), reported in Eq. (13a), and the logarithmic error for each data point as described in Eq. (13b) coherently with previous research on the topic [46,95,96]. Lower values of SMAPE indicate closer match between experimental and numerical results, while the logarithmic errors were manipulated through the use of kernel density estimations. The obtained results of logarithmic errors are shown in Fig. 19(e). It is worth noting that the predictions using FSCFs at 99th percentile shows better accuracy than the corresponding ones obtained through the use of FSCFs at 95th percentile confirming the findings of [91]. Besides accuracy, predictions using FSCFs at 95th percentile were also less conservative than the corresponding ones obtained with FSCFs at 99th percentile as shown in Fig. 19(e). Another aspect to be discussed concerns the validity of the proposed procedure.

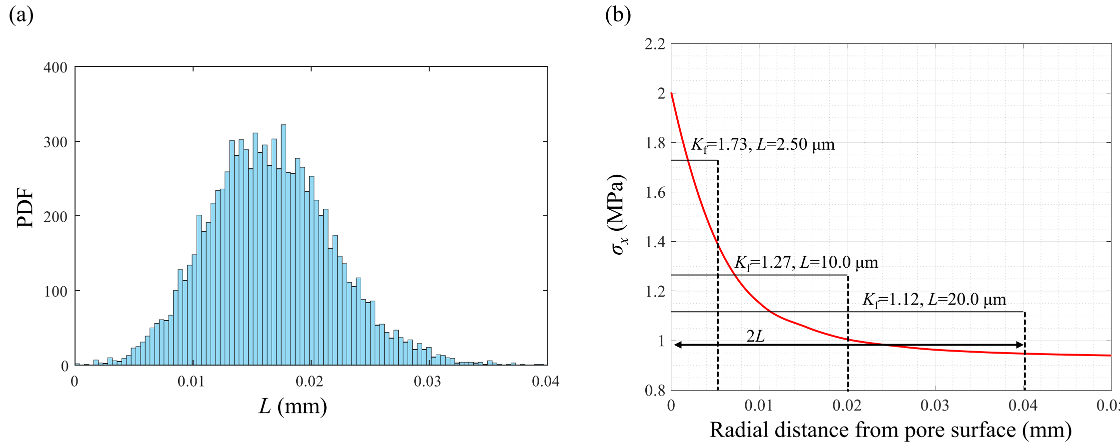

Fig. 16. (a) Histogram showing a representative example of the statistical distribution of the critical distance L at a certain number of cycles to failure N_f and (b) explanatory example of the high dependence between the FSCFs of pores $K_{f,pore}$ and the values of L.

Table 11
Deepest valley distance from mean profile h_p and pore diameter D both at 99th percentile and pore distance from external surface d at 1st percentile for all the specimens.

Specimen	h_p (99%) (μm)	D (99%) (μm)	d (1%) (μm)
Plain cyclone	33.4	101	3.41
VR1 cyclone	206	118	2.98
VR03 cyclone	314	92.1	1.97
Plain Fenice	34.8	65.7	0.82
VR1 Fenice	215	137	2.39
VR03 Fenice	340	160	2.16

In fact, the FSCFs of pores and surface roughness were conservatively multiplied by supposing an interaction between the two effects. A range of validity was proposed by taking inspiration from [35,97] and BS 7910 where it is recommended that the effects of porosities and surface roughness can be combined if the distance between deepest surface valley and pore is smaller than the minimum between pore diameter and roughness valley. Considering the statistical analysis of internal defects and surface roughness implemented in this work, the constraint of [35] was reformulated, and the proposed computational approach can be considered valid if the pore distance from external surface d at 1st percentile is smaller than the minimum between the values of h_p and pore diameter D both calculated at 99th percentile. The corresponding results for each kind of specimen analysed in the current work are presented in Table 11. Finally, it is important to remark the fundamental role played by the size effect, in fact, in the plain specimens the ratios between HSV and V_0 and between HSS and S_0 were much higher than 1, while in the VR03 specimens the corresponding values were lower than 1. As a consequence, neglecting the size effect could lead to overestimate or underestimate the FSCFs.

$$K_{f,hard} = \frac{HV_{av,v} - \sigma_{HV,v}}{HV_{av,c} - \sigma_{HV,c}} \tag{12a}$$

$$K_{f,tot} = K_{f,pore}\,(99\%)\,K_{f,rough}\,(99\%)\,K_{f,hard} \tag{12b}$$

$$\sigma_{a,pred} = \sigma_a^* / K_{f,tot} \tag{12c}$$

$$\text{SMAPE} = \frac{100}{N}\sum_{i=1}^{N}\frac{\left|N_{f,exp,i} - N_{f,pred,i}\right|}{N_{f,exp,i} + N_{f,pred,i}} \tag{13a}$$

$$E_{Log.,i} = \text{Log}\left(\frac{N_{f,exp,i}}{N_{f,pred,i}}\right) \tag{13b}$$

4. Conclusions

This study investigated the fatigue behaviour of LPBF Inconel 718 manufactured from sustainable powder feedstocks, combining experimental characterization with a unified modelling framework based on TCD, EVS, FE simulations, and CSMs.

- The experimental results demonstrated that the use of two different partially recycled powders leads to only moderate variations in mechanical performance, with Fenice specimens showing slightly lower strength but higher ductility compared to cyclone specimens. These differences were consistently explained by variations in chemical composition, i.e. the ratio of Fe, Cr, Mo, Nb, Ti and Al to Ni, and powder characteristics such as flowability and PSD, confirming the feasibility of using recycled feedstocks without significant degradation of fatigue performance.
- Fractographic and statistical analyses showed that fatigue crack initiation is governed by surface roughness, while pores play a secondary role, particularly when located near the free surface. This behaviour was supported by FE simulations, which indicated that FSCFs associated with surface roughness are higher than those associated with pores.
- The proposed modelling framework provides a unified approach that combines FE, EVS, TCD, and CSMs to predict the combined effects of surface roughness, internal porosity, notch geometry, and size effect, achieving high R^2 values (around 90% by using FSCFS at 99th percentile) and demonstrating both robustness and reliability. On the contrary, the use of FSCFs at 95th percentile provided less accurate and less conservative results. The integration of CSMs enabled efficient evaluation over a wide defect-parameter space, while the use of EVS allowed a robust representation of the most detrimental defects. Sensitivity analyses further showed that the critical distance is the dominant parameter influencing model predictions, while the relative importance of pore size and location depends on the specimen geometry.
- It is important to remark that the effectiveness of the proposed framework is linked to the nature of the defect population. In the present study, pores were predominantly near-spherical gas-induced defects, as confirmed by metallographic analyses. This condition is representative of well-optimized LPBF process parameters, where lack-of-fusion defects are minimized. Under these circumstances, metallographic characterization combined

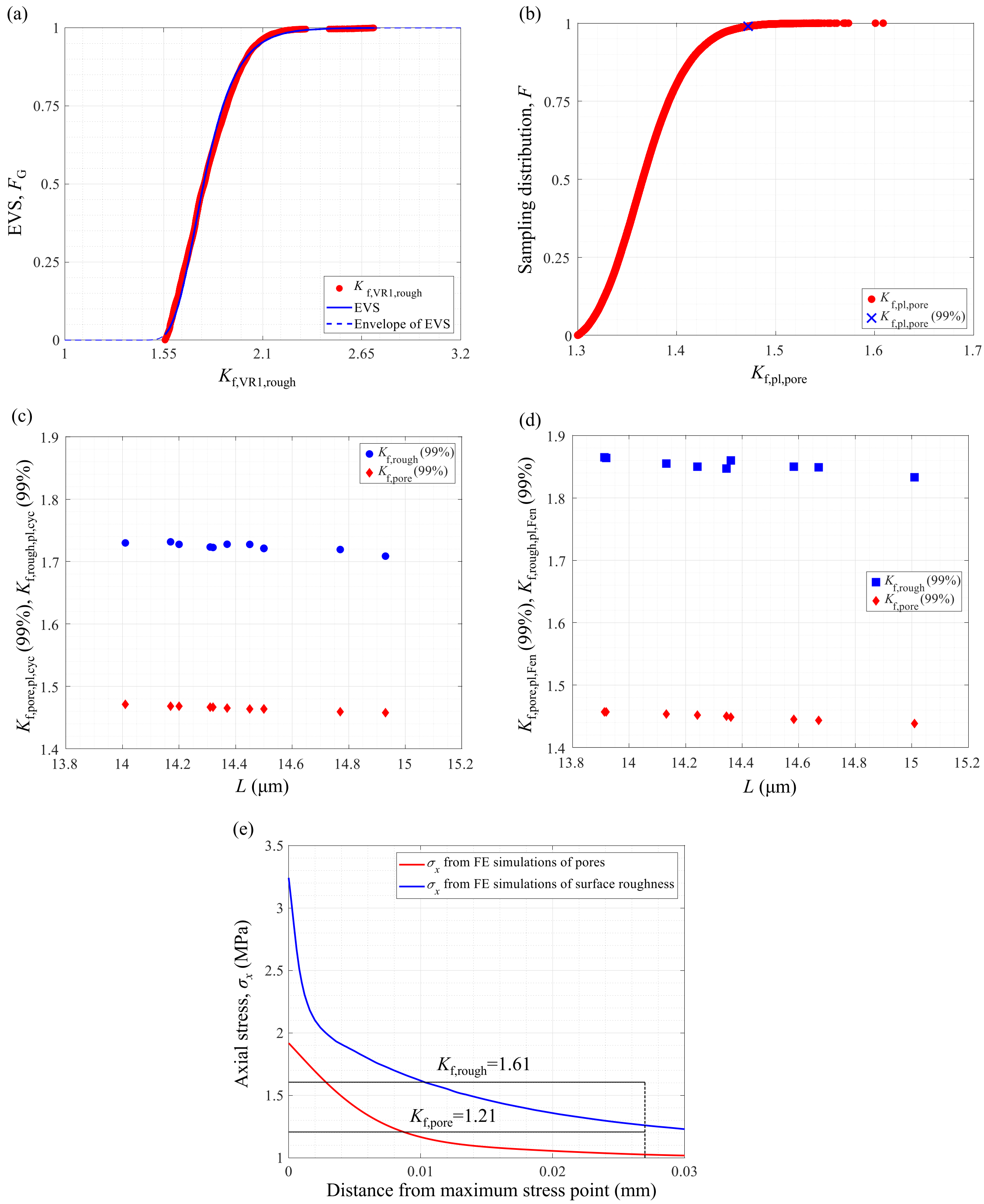

Fig. 17. Explanatory examples of (a) sampling distribution of FSCFs, for VR1 specimens, provided by the surface roughness with corresponding fitted EVS, (b) obtained sampling distribution through the ANN to calculate FSCFs of pores at 99th percentile in plain specimens, comparison between FSCFs at 99th percentile of pores and surface roughness for (c) cyclone and (d) Fenice plain specimens and (e) example of the differences between stress distributions and corresponding FSCFs, according to LM and with L = 13.5 μm, provided by surface roughness and pores in plain specimens.

with continuum-scale modelling provides a reliable description of defect-driven fatigue behaviour. In the presence of irregular lack-of-fusion defects or highly anisotropic defect morphologies, additional characterization and modelling efforts may be required.

- Beyond the methodological contribution, the results provide important insights into the applicability of sustainable powder feedstocks. The findings demonstrate that partially recycled powders can be employed while maintaining reliable and predictable fatigue performance, provided that process parameters are properly optimized and defect populations are controlled. The proposed framework supports this transition by enabling a quantitative and efficient assessment of fatigue behaviour, offering a scalable tool for qualification and certification. Overall, sustainable powder feedstocks emerge as a promising pathway towards more resource-efficient additive manufacturing, when combined with robust defect-aware design and assessment methodologies.

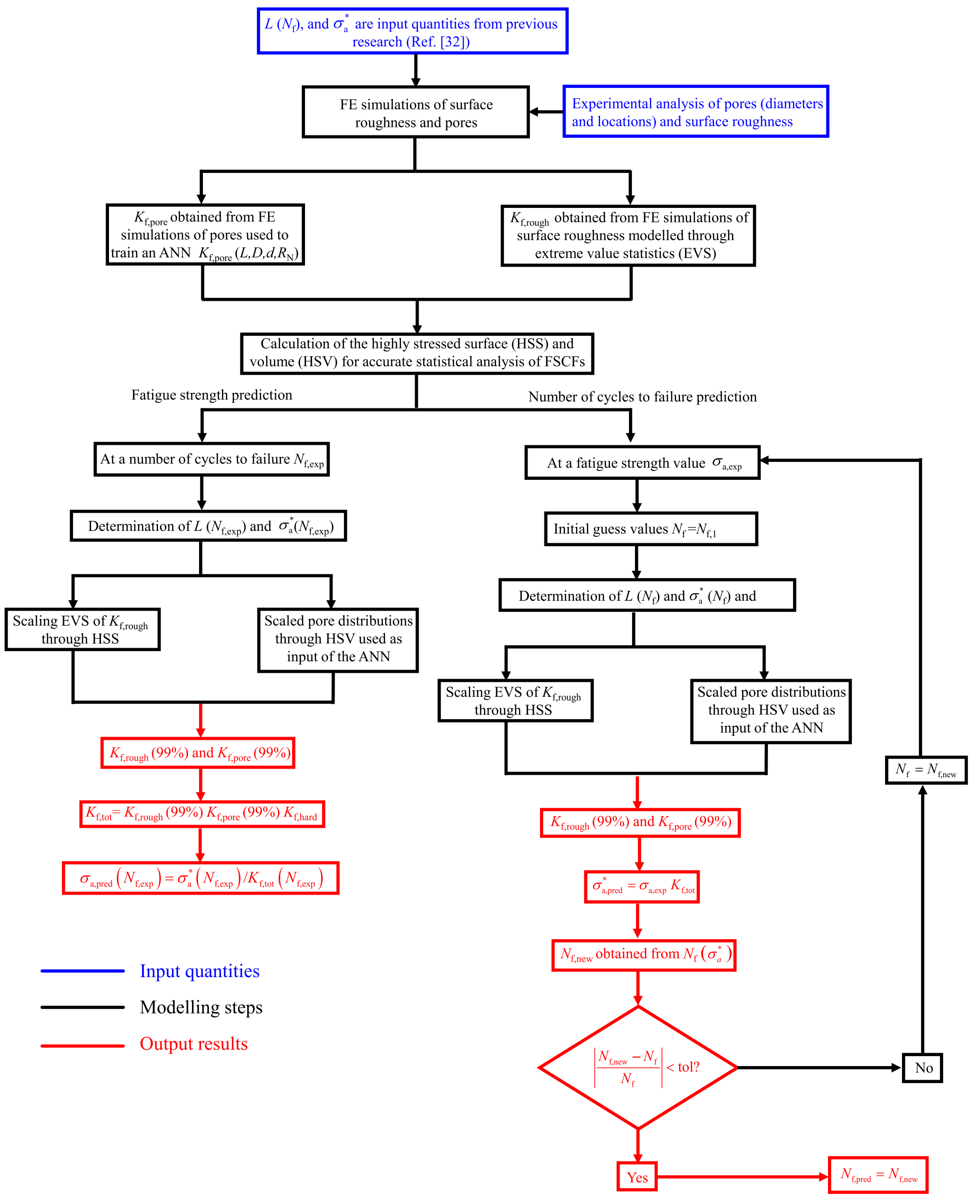

Fig. 18. Logic flow of the implemented procedure.

CRediT authorship contribution statement

L. Romanelli: Writing – review & editing, Writing – original draft, Visualization, Validation, Software, Methodology, Investigation, Formal analysis, Data curation, Conceptualization. **C. Santus:** Writing – review & editing, Supervision, Methodology. **G. Macoretta:** Writing – review & editing, Methodology, Investigation, Data curation, Conceptualization. **B.D. Monelli:** Writing – review & editing, Supervision, Project administration, Methodology, Funding acquisition. **H. Rajaei:** Writing – review & editing, Writing – original draft, Methodology, Investigation, Data curation. **C. Menapace:** Writing – review & editing, Writing – original draft, Supervision, Methodology, Investigation, Data curation, Conceptualization. **M. Benedetti:** Writing – review & editing, Writing – original draft, Visualization, Supervision, Software, Project administration, Methodology, Investigation, Funding acquisition, Data curation, Conceptualization.

Funding and acknowledgements

This work was Funded by the European Union - Next Generation EU and supported by the Italian Ministry of University and Research (MUR) in the frame of the programme PNRR_Piano Nazionale di Ripresa e Resilienza – MISSIONE 4 COMPONENTE 2, "Dalla ricerca all'impresa" INVESTIMENTO 1.1, "Fondo per il Programma Nazionale di Ricerca e Progetti di Rilevante Interesse Nazionale (PRIN)", project title "RePowder: recycled powder for sustainable metal additive manufacturing", grant number P2022MEFCJ. Website of the project: https://www.repowder.it/

Declaration of competing interest

The authors declare that they have no known competing financial interests or personal relationships that could have appeared to influence the work reported in this paper.

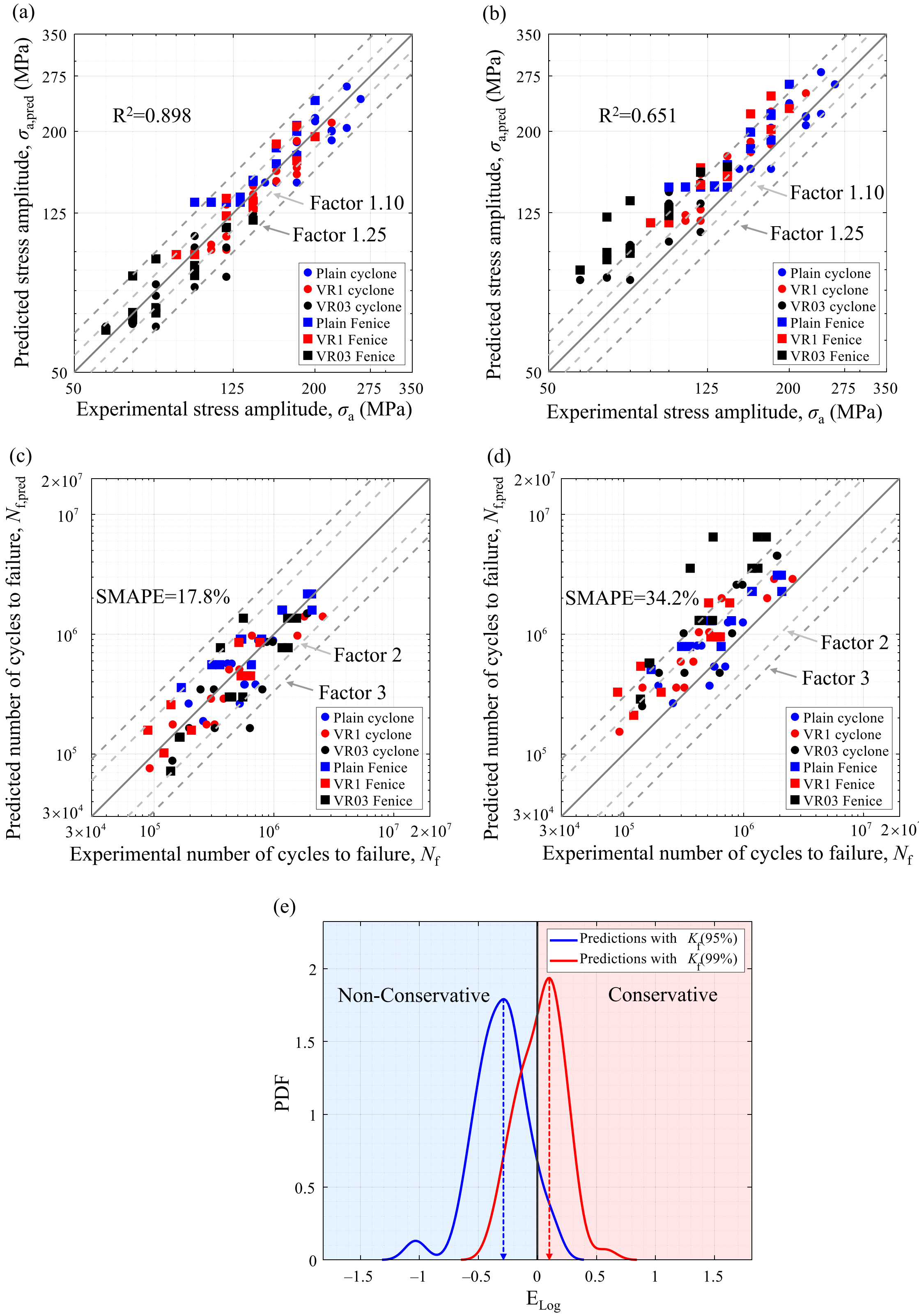

Fig. 19. Comparisons between predicted and experimental fatigue strength values using (a) FSCFs at 99th percentile, (b) FSCFs at 95th percentile and comparisons between predicted and experimental number of cycles to failure values using (c) FSCFs at 99th percentile and (d) FSCFs at 95th percentile. (e) PDF of logarithmic errors of number of cycles to failure using FSCFs at 99th and 95th percentiles.

Data availability

Data will be made available on request.

References

[1] M.A. Iqbal, K. Skotnicová, A. Shafiq, T.N. Sindhu, Inconel alloys: A comprehensive review of properties and advanced manufacturing techniques, Int. J. Thermofluids 29 (2025) 101394, http://dx.doi.org/10.1016/j.ijft.2025.101394.

[2] S. Dhiman, R.S. Joshi, S. Singh, S.S. Gill, H. Singh, R. Kumar, V. Kumar, A framework for effective and clean conversion of machining waste into metal powder feedstock for additive manufacturing, Clean. Eng. Technol. 4 (2021) 100151, http://dx.doi.org/10.1016/j.clet.2021.100151.

[3] M. Benedetti, M. Perini, M. Vanazzi, A. Giorgini, G. Macoretta, C. Menapace, Atomized scrap powder feedstock for sustainable inconel 718 additive manufacturing via LPBF: a study of static and fatigue properties, Prog. Addit. Manuf. 9 (6) (2023) 1843–1856, http://dx.doi.org/10.1007/s40964-023-00547-z.

[4] M. Ganta, M. Kurek, A. Emdadi, T. Łagoda, M. Pagáč, Effect of powder recycling on powder characteristics and mechanical properties of materials produced by laser powder bed fusion (LPBF): A review, Sustain. Mater. Technol. 46 (2025) e01714, http://dx.doi.org/10.1016/j.susmat.2025.e01714.

[5] N.E. Gorji, R. O'Connor, A. Mussatto, M. Snelgrove, P.G.M. González, D. Brabazon, Recyclability of stainless steel (316L) powder within the additive manufacturing process, Materialia 8 (2019) 100489, http://dx.doi.org/10.1016/j.mtla.2019.100489.

[6] P.C. Priarone, F.S. Gobber, S. Cacace, Parametric modeling of cradle-to-gate carbon emissions from gas-atomized AISI 316L powders under closed-loop feedstock strategies, Powder Technol. 470 (2026) 121949, http://dx.doi.org/10.1016/j.powtec.2025.121949.

[7] M. Cabrioli, M. Silva C., S. Gholamzadeh, M. Vanazzi, S. Amirabdollahian, M. Perini, W. Łacisz, B. Kalicki, Upcycling of copper scrap into high-quality powder for additive manufacturing: Processing, characterization, and sustainability assessment, J. Manuf. Mater. Process. 9 (9) (2025) 320, http://dx.doi.org/10.3390/jmmp9090320.

[8] S. Ding, V. Pusateri, T. Dahmen, C. Semarak, V.K. Nadimpalli, C. Cimpan, Life cycle assessment of metallurgical options for recycling high-alloy tool steels, Resour. Conserv. Recycl. 226 (2026) 108655, http://dx.doi.org/10.1016/j.resconrec.2025.108655.

[9] C. Monti, F.S. Gobber, M. Turani, K. Papis, P.C. Priarone, M. Actis Grande, M. Bambach, Evaluating the use of scrap metal to produce Al-5Cu-3Ti-1Cr-1Fe alloy powder for laser powder bed fusion, Sustain. Mater. Technol. 45 (2025) e01606, http://dx.doi.org/10.1016/j.susmat.2025.e01606.

[10] G. Locatelli, S. Bocchi, M. Quarto, G. D'Urso, Laser powder bed fusion of atomized industrial waste-derived inconel 725 alloy powders: A machine learning-assisted process optimization, Mater. Sci. Addit. Manuf. 5 (1) (2025) 025320072, http://dx.doi.org/10.36922/msam025320072.

[11] H.K. Bajaj, M. Sojoodi, F.Y. Asare Baffour, M. Hesami, S. Houshmand, V.R. De Silva Kanakaratne, A. Celebi, M. Elahinia, Sustainable pathways in powder reuse: A comparative study of virgin, reused, and ultrasonic-atomization-recycled NiTi powder for additive manufacturing, Sustainability 18 (4) (2026) 1843, http://dx.doi.org/10.3390/su18041843.

[12] W.Y. Leong, Circular economy through green additive manufacturing in medical device manufacturing, in: ECBIOS 2025, in: ECBIOS 2025, MDPI, 2026, p. 1, http://dx.doi.org/10.3390/engproc2026129001.

[13] J.-S. Ludger Bernsmann, J.H. Schleifenbaum, From construction for construction: Additive manufacturing with gas-atomized recycled steel scrap, Circ. Econ. 4 (3) (2025) 100157, http://dx.doi.org/10.1016/j.cec.2025.100157.

[14] H. Tupac-Yupanqui, A. Armani, Selective laser melting and mechanical characterization of superalloys made from recycled parts, Procedia CIRP 126 (2024) 621–626, http://dx.doi.org/10.1016/j.procir.2024.08.250.

[15] H. Tupac-Yupanqui, A. Armani, Additive manufacturing of functional inconel 718 parts from recycled materials, J. Mater. Eng. Perform. 30 (2) (2021) 1177–1187, http://dx.doi.org/10.1007/s11665-020-05402-8.

[16] G.E. Bean, D.B. Witkin, T.D. McLouth, D.N. Patel, R.J. Zaldivar, Effect of laser focus shift on surface quality and density of inconel 718 parts produced via selective laser melting, Addit. Manuf. 22 (2018) 207–215, http://dx.doi.org/10.1016/j.addma.2018.04.024.

[17] M.R. Khosravani, F. Berto, M.R. Ayatollahi, T. Reinicke, Fracture behavior of additively manufactured components: A review, Theor. Appl. Fract. Mech. 109 (2020) 102763, http://dx.doi.org/10.1016/j.tafmec.2020.102763.

[18] X. Wang, L. Xu, L. Zhao, Y. Han, Evaluation of defect-related fatigue performance of additive manufacturing GH4169 via small punch test, Theor. Appl. Fract. Mech. 128 (2023) 104162, http://dx.doi.org/10.1016/j.tafmec.2023.104162.

[19] J. Gockel, L. Sheridan, B. Koerper, B. Whip, The influence of additive manufacturing processing parameters on surface roughness and fatigue life, Int. J. Fatigue 124 (2019) 380–388, http://dx.doi.org/10.1016/j.ijfatigue.2019.03.025.

[20] G. Macoretta, L. Romanelli, C. Santus, L. Romoli, A.H.A. Lutey, F. Uriati, G. Nicoletto, S. Raghavendra, M. Benedetti, B.D. Monelli, Modelling of the surface morphology and size effects on fatigue strength of L-PBF inconel 718 by comparing different testing specimens, Int. J. Fatigue 181 (2024) 108120, http://dx.doi.org/10.1016/j.ijfatigue.2023.108120.

[21] C. Guo, S. Li, S. Shi, X. Li, X. Hu, Q. Zhu, R.M. Ward, Effect of processing parameters on surface roughness, porosity and cracking of as-built IN738LC parts fabricated by laser powder bed fusion, J. Mater. Process. Technol. 285 (2020) 116788, http://dx.doi.org/10.1016/j.jmatprotec.2020.116788.

[22] F. Uriati, G. Nicoletto, A.H.A. Lutey, As-built surface quality and fatigue resistance of inconel 718 obtained by additive manufacturing, Mater. Des. Process. Commun. 3 (4) (2021) http://dx.doi.org/10.1002/mdp2.228.

[23] S.O. Alfred, M. Amiri, High-temperature fatigue of additively manufactured inconel 718: A short review, J. Eng. Mater. Technol. 147 (1) (2024) http://dx.doi.org/10.1115/1.4066048.

[24] M. Matušů, B. Roidl, S. Amann, J. Rosenthal, I. Zetková, M. Zetek, Fatigue behaviour and S-N curve prediction of additively manufactured inconel 718 using self-heating and energy-based methods, Eng. Fail. Anal. 174 (2025) 109507, http://dx.doi.org/10.1016/j.engfailanal.2025.109507.

[25] D. Sommer, B. Truetsch, C. Esen, R. Hellmann, Effect of hot isostatic pressing and sequenced heat treatment on the mechanical properties of hybrid additive manufactured inconel 718 components, J. Manuf. Mater. Process. 9 (11) (2025) 378, http://dx.doi.org/10.3390/jmmp9110378.

[26] C. Santus, L. Romanelli, T. Grossi, P. Neri, L. Romoli, A.H.A. Lutey, M. Pedranz, M. Benedetti, Torsional-loaded notched specimen fatigue strength prediction based on mode I and mode III critical distances and fracture surface investigations with a 3D optical profilometer, Int. J. Fatigue 161 (2022) 106913, http://dx.doi.org/10.1016/j.ijfatigue.2022.106913.

[27] W. Macek, R. Masoudi Nejad, S.-P. Zhu, J. Trembacz, R. Branco, J.D.M. Costa, J.A.M. Fereira, C. Capela, Effect of bending-torsion on fracture and fatigue life for 18Ni300 steel specimens produced by SLM, Mech. Mater. 178 (2023) 104576, http://dx.doi.org/10.1016/j.mechmat.2023.104576.

[28] M. Pellizzari, B. AlMangour, M. Benedetti, S. Furlani, D. Grzesiak, F. Deirmina, Effects of building direction and defect sensitivity on the fatigue behavior of additively manufactured H13 tool steel, Theor. Appl. Fract. Mech. 108 (2020) 102634, http://dx.doi.org/10.1016/j.tafmec.2020.102634.

[29] B. Bostan, S. Hinnebusch, D. Anderson, A.C. To, Accurate detection of local porosity in laser powder bed fusion through deep learning of physics-based in-situ infrared camera signatures, Addit. Manuf. 101 (2025) 104701, http://dx.doi.org/10.1016/j.addma.2025.104701.

[30] K.S. Stopka, A. Desrosiers, T. Nicodemus, N. Krutz, A. Andreaco, M.D. Sangid, Intentionally seeding pores in additively manufactured alloy 718: Process parameters, microstructure, defects, and fatigue, Addit. Manuf. 66 (2023) 103450, http://dx.doi.org/10.1016/j.addma.2023.103450.

[31] H. Masuo, Y. Tanaka, S. Morokoshi, H. Yagura, T. Uchida, Y. Yamamoto, Y. Murakami, Influence of defects, surface roughness and HIP on the fatigue strength of Ti-6Al-4V manufactured by additive manufacturing, Int. J. Fatigue 117 (2018) 163–179, http://dx.doi.org/10.1016/j.ijfatigue.2018.07.020.

[32] L. Romanelli, C. Santus, G. Macoretta, M. Barsanti, B.D. Monelli, I. Senegaglia, A.H.A. Lutey, H. Rajaei, C. Menapace, M. Benedetti, A TCD-based statistical method to assess the impact of surface roughness and pores on the fatigue strength of LPBF inconel 718 specimens, Int. J. Fatigue 194 (2025) 108821, http://dx.doi.org/10.1016/j.ijfatigue.2025.108821.

[33] D. Celli, L. Sheridan, T. George, J. Warner, L. Smith, Forecasting high cycle and very high cycle fatigue through enhanced strain-energy based fatigue life prediction, in: Volume 10B: Structures and Dynamics — Fatigue, Fracture, and Life Prediction; Probabilistic Methods; Rotordynamics; Structural Mechanics and Vibration, in: GT2024, American Society of Mechanical Engineers, 2024, http://dx.doi.org/10.1115/gt2024-129455.

[34] Y. Murakami, Inclusion rating by statistics of extreme values and its application to fatigue strength prediction and quality control of materials, J. Res. Natl. Inst. Stand. Technol. 99 (4) (1994) 345, http://dx.doi.org/10.6028/jres.099.032.

[35] Y. Murakami, Metal Fatigue, Elsevier, 2019, http://dx.doi.org/10.1016/c2016-0-05272-5.

[36] S. Vantadori, C. Ronchei, D. Scorza, A. Zanichelli, A novel analytical procedure for fatigue strength assessment and lifetime estimation of AM metallic components, Eng. Fail. Anal. 152 (2023) 107480, http://dx.doi.org/10.1016/j.engfailanal.2023.107480.

[37] C. Santus, L. Romanelli, L. Bertini, A. Burchianti, T. Inoue, Resonant fatigue tests on polished drill pipe specimens, Machines 12 (5) (2024) 314, http://dx.doi.org/10.3390/machines12050314.

[38] F. Farhad, S. Murchio, M. Babaei, A. Albertini, D. Maniglio, F. Berto, M. Benedetti, Corrosion-fatigue of L-PBF Ti-6Al-4V lattice struts: role of geometrical imperfections under simulated physiological conditions, Int. J. Fatigue 211 (2026) 109747, http://dx.doi.org/10.1016/j.ijfatigue.2026.109747.

[39] D. Rigon, F. Coppola, G. Meneghetti, Fracture mechanics-based analysis of the fatigue limit of Ti6Al4V alloy specimens manufactured by SLM in as-built surface conditions by means of areal measurements, Eng. Fract. Mech. 295 (2024) 109720, http://dx.doi.org/10.1016/j.engfracmech.2023.109720.

[40] G. Macoretta, L. Bertini, B.D. Monelli, F. Berto, Productivity-oriented SLM process parameters effect on the fatigue strength of inconel 718, Int. J. Fatigue 168 (2023) 107384, http://dx.doi.org/10.1016/j.ijfatigue.2022.107384.

[41] A. Sapora, P. Cornetti, A. Campagnolo, G. Meneghetti, Fatigue limit: Crack and notch sensitivity by finite fracture mechanics, Theor. Appl. Fract. Mech. 105 (2020) 102407, http://dx.doi.org/10.1016/j.tafmec.2019.102407.

[42] X. Shen, D. Zeng, L. Lu, Investigating the effect of notch size on critical distance and fatigue limit by coupling the theory of critical distance and finite fracture mechanics, Theor. Appl. Fract. Mech. 122 (2022) 103566, http://dx.doi.org/10.1016/j.tafmec.2022.103566.

[43] M. Sánchez, S. Cicero, S. Arrieta, V. Martínez, Fracture load predictions in additively manufactured ABS U-notched specimens using average strain energy density criteria, Materials 15 (7) (2022) 2372, http://dx.doi.org/10.3390/ma15072372.

[44] W. Macek, R. Branco, J. de Jesus, J.D. Costa, S.-P. Zhu, R. Masoudi Nejad, A. Gryguć, Strain energy density and entire fracture surface parameters relationship for LCF life prediction of additively manufactured 18Ni300 steel, Int. J. Damage Mech. 33 (9) (2024) 725–747, http://dx.doi.org/10.1177/10567895241245879.

[45] R. De Biasi, L. Romanelli, C. Santus, M. Perini, F. Berto, M. Benedetti, Fatigue life prediction of multi jet fusion-manufactured polyamide12 lattice structures using the average strain energy density method, Int. J. Fatigue 206 (2026) 109452, http://dx.doi.org/10.1016/j.ijfatigue.2025.109452.

[46] A.M. Mirzaei, A.H. Mirzaei, A. Sapora, P. Cornetti, Strain based finite fracture mechanics for fatigue life prediction of additively manufactured samples, Int. J. Fract. 249 (3) (2025) http://dx.doi.org/10.1007/s10704-025-00855-1.

[47] D. Taylor, The Theory of Critical Distances, Elsevier Science, 2007, p. 306, http://dx.doi.org/10.1016/B978-0-08-044478-9.X5000-5.

[48] D. Taylor, The theory of critical distances: A link to micromechanisms, Theor. Appl. Fract. Mech. 90 (2017) 228–233, http://dx.doi.org/10.1016/j.tafmec.2017.05.018.

[49] A.R. Torabi, S. Shahbaz, S. Mohammadi, Can the family of equivalent material concept successfully estimate the critical stress of nonlinear materials provided by the theory of critical distances? Theor. Appl. Fract. Mech. 143 (2026) 105500, http://dx.doi.org/10.1016/j.tafmec.2026.105500.

[50] L. Susmel, D. Taylor, A critical distance/plane method to estimate finite life of notched components under variable amplitude uniaxial/multiaxial fatigue loading, Int. J. Fatigue 38 (2012) 7–24, http://dx.doi.org/10.1016/j.ijfatigue.2011.11.015.

[51] C. Santus, L. Romanelli, T. Grossi, L. Bertini, L. Le Bone, F. Chiesi, L. Tognarelli, Elastic–plastic analysis of high load ratio fatigue tests on a shot-peened quenched and tempered steel, combining the chaboche model and the theory of critical distances, Int. J. Fatigue 174 (2023) 107713, http://dx.doi.org/10.1016/j.ijfatigue.2023.107713.

[52] L. Susmel, D. Taylor, Estimating lifetime of notched components subjected to variable amplitude fatigue loading according to the elastoplastic theory of critical distances, J. Eng. Mater. Technol. 137 (1) (2015) http://dx.doi.org/10.1115/1.4028927.

[53] M.R. Ayatollahi, A.R. Torabi, B. Bahrami, On the necessity of using critical distance model in mixed mode brittle fracture prediction of V-notched Brazilian disk specimens under negative mode I conditions, Theor. Appl. Fract. Mech. 84 (2016) 38–48, http://dx.doi.org/10.1016/j.tafmec.2016.01.001.

[54] V. Madrazo, S. Cicero, I. Carrascal, On the application of the theory of critical distances to the structural integrity assessment of stress risers, Int. J. Struct. Integr. 4 (2) (2013) 219–239, http://dx.doi.org/10.1108/17579861311321708.

[55] V. Madrazo, S. Cicero, T. García, Assessment of notched structural steel components using failure assessment diagrams and the theory of critical distances, Eng. Fail. Anal. 36 (2014) 104–120, http://dx.doi.org/10.1016/j.engfailanal.2013.09.012.

[56] S.V. Suknev, Extending the theory of critical distances to quasi-brittle fracture, Theor. Appl. Fract. Mech. 114 (2021) 102996, http://dx.doi.org/10.1016/j.tafmec.2021.102996.

[57] R. Hao, P. Lehto, W. Lin, Critical distance-based fatigue life evaluation of blunt notch details in steel bridges, J. Constr. Steel Res. 201 (2023) 107738, http://dx.doi.org/10.1016/j.jcsr.2022.107738.

[58] J. Sun, P. Li, L. Susmel, The theory of critical distances for random vibration fatigue life analysis of notched specimens, Fatigue Fract. Eng. Mater. Struct. 46 (10) (2023) 3610–3621, http://dx.doi.org/10.1111/ffe.14088.

[59] P. Li, L. Susmel, M. Ma, The life prediction of notched aluminum alloy specimens after laser shock peening by TCD, Int. J. Fatigue 176 (2023) 107795, http://dx.doi.org/10.1016/j.ijfatigue.2023.107795.

[60] S. Cicero, Assessment of structural materials containing notch-type defects: A comprehensive validation of the FAD-TCD methodology on metallic and non-metallic materials, Theor. Appl. Fract. Mech. 133 (2024) 104612, http://dx.doi.org/10.1016/j.tafmec.2024.104612.

[61] D. Morgan, S. Quinlan, D. Taylor, Using the theory of critical distances to predict notch effects in fibre composites, Theor. Appl. Fract. Mech. 118 (2022) 103285, http://dx.doi.org/10.1016/j.tafmec.2022.103285.

[62] G. Cortabitarte, I. Llavori, J.A. Esnaola, S. Blasón, M. Larrañaga, J. Larrañaga, A. Arana, I. Ulacia, Application of the theory of critical distances for fatigue life assessment of spur gears, Theor. Appl. Fract. Mech. 128 (2023) 104086, http://dx.doi.org/10.1016/j.tafmec.2023.104086.

[63] J.A. Araújo, L. Susmel, D. Taylor, J.C.T. Ferro, J.L.A. Ferreira, On the prediction of high-cycle fretting fatigue strength: Theory of critical distances vs. hot-spot approach, Eng. Fract. Mech. 75 (7) (2008) 1763–1778, http://dx.doi.org/10.1016/j.engfracmech.2007.03.026.

[64] D. Infante-Garcia, A. Zabala, E. Giner, I. Llavori, On the use of the theory of critical distances with mesh control for fretting fatigue life assessment in complete and nearly complete contacts, Theor. Appl. Fract. Mech. 121 (2022) 103476, http://dx.doi.org/10.1016/j.tafmec.2022.103476.

[65] J. Justo, J. Castro, S. Cicero, M.A. Sánchez-Carro, R. Husillos, Notch effect on the fracture of several rocks: Application of the theory of critical distances, Theor. Appl. Fract. Mech. 90 (2017) 251–258, http://dx.doi.org/10.1016/j.tafmec.2017.05.025.

[66] A.A. Ahmed, L. Susmel, A material length scale–based methodology to assess static strength of notched additively manufactured polylactide (PLA), Fatigue Fract. Eng. Mater. Struct. 41 (10) (2018) 2071–2098, http://dx.doi.org/10.1111/ffe.12746.

[67] T.D. Dinh, J. Vanwalleghem, H. Xiang, H. Erdelyi, T. Craeghs, W.V. Paepegem, A unified approach to model the effect of porosity and high surface roughness on the fatigue properties of additively manufactured Ti6-Al4-V alloys, Addit. Manuf. 33 (2020) 101139, http://dx.doi.org/10.1016/j.addma.2020.101139.

[68] S. Cicero, S. Arrieta, M. Sánchez, L. Castanon-Jano, Using the point method to estimate failure loads in 3D printed graphene-reinforced PLA notched plates, J. Phys.: Conf. Ser. 2692 (1) (2024) 012043, http://dx.doi.org/10.1088/1742-6596/2692/1/012043.

[69] L. Susmel, Theory of critical distances and notched filament-based 3D-printed components: lessons learned from polymers and concrete, Procedia Struct. Integr. 53 (2024) 44–51, http://dx.doi.org/10.1016/j.prostr.2024.01.006.

[70] M.F. Yaren, L. Susmel, A novel critical distance-based homogenised material approach to estimate fatigue lifetime of plain/notched polylactide 3D-printed with different in-fill levels, Int. J. Fatigue 193 (2025) 108750, http://dx.doi.org/10.1016/j.ijfatigue.2024.108750.

[71] M.F. Yaren, L. Susmel, A homogenised material approach to predict fatigue life of additively manufactured PLA with different in-fill levels, Procedia Struct. Integr. 76 (2026) 99–106, http://dx.doi.org/10.1016/j.prostr.2025.12.292.

[72] L. Susmel, Estimating notch fatigue limits via a machine learning-based approach structured according to the classic Kf formulas, Int. J. Fatigue 179 (2024) 108029, http://dx.doi.org/10.1016/j.ijfatigue.2023.108029.

[73] W.Q. Hao, L. Tan, X.G. Yang, D.Q. Shi, M.L. Wang, G.L. Miao, Y.S. Fan, A physics-informed machine learning approach for notch fatigue evaluation of alloys used in aerospace, Int. J. Fatigue 170 (2023) 107536, http://dx.doi.org/10.1016/j.ijfatigue.2023.107536.

[74] A. Karolczuk, A. Kurek, Machine learning insight into the mean stress impact on fatigue life of additively manufactured 18ni300 maraging steel under various multiaxial stress paths, Int. J. Fatigue 198 (2025) 109023, http://dx.doi.org/10.1016/j.ijfatigue.2025.109023.

[75] E. Salvati, A. Tognan, L. Laurenti, M. Pelegatti, F. De Bona, A defect-based physics-informed machine learning framework for fatigue finite life prediction in additive manufacturing, Mater. Des. 222 (2022) 111089, http://dx.doi.org/10.1016/j.matdes.2022.111089.

[76] A. Centola, A. Ciampaglia, D.S. Paolino, A. Tridello, Probabilistic machine learning for preventing fatigue failures in additively manufactured SS316L, Eng. Fail. Anal. 168 (2025) 109081, http://dx.doi.org/10.1016/j.engfailanal.2024.109081.

[77] D. Perghem, B. Salehnasab, S. Beretta, S. Shao, N. Shamsaei, ML-based detection of critical defects in additively manufactured parts via X-ray computed tomography, Mater. Des. 260 (2025) 115184, http://dx.doi.org/10.1016/j.matdes.2025.115184.

[78] M. Moda, A. Chiocca, G. Macoretta, B.D. Monelli, L. Bertini, Technological implications of the rosenthal solution for a moving point heat source in steady state on a semi-infinite solid, Mater. Des. 223 (2022) 110991, http://dx.doi.org/10.1016/j.matdes.2022.110991.

[79] D. Zhang, W. Niu, X. Cao, Z. Liu, Effect of standard heat treatment on the microstructure and mechanical properties of selective laser melting manufactured inconel 718 superalloy, Mater. Sci. Eng.: A 644 (2015) 32–40, http://dx.doi.org/10.1016/j.msea.2015.06.021.

[80] M. Shahabi, T. Reddy, A.D. Rollett, S.P. Narra, A statistical approach to determine data requirements for part porosity characterization in laser powder bed fusion additive manufacturing, Mater. Charact. 190 (2022) 112027, http://dx.doi.org/10.1016/j.matchar.2022.112027.

[81] E. Hosseini, V.A. Popovich, A review of mechanical properties of additively manufactured inconel 718, Addit. Manuf. 30 (2019) 100877, http://dx.doi.org/10.1016/j.addma.2019.100877.

[82] M.E. Aydinöz, F. Brenne, M. Schaper, C. Schaak, W. Tillmann, J. Nellesen, T. Niendorf, On the microstructural and mechanical properties of post-treated additively manufactured inconel 718 superalloy under quasi-static and cyclic loading, Mater. Sci. Eng.: A 669 (2016) 246–258, http://dx.doi.org/10.1016/j.msea.2016.05.089.

[83] A. Segerstark, J. Andersson, L.-E. Svensson, O. Ojo, Microstructural characterization of laser metal powder deposited alloy 718, Mater. Charact. 142 (2018) 550–559, http://dx.doi.org/10.1016/j.matchar.2018.06.020.

[84] D. Sindhura, M.V. Sravya, G.V.S. Murthy, Comprehensive microstructural evaluation of precipitation in inconel 718, Met. Microstruct. Anal. 8 (2) (2019) 233–240, http://dx.doi.org/10.1007/s13632-018-00513-0.

[85] H. Guan, W. Jiang, J. Lu, Y. Zhang, Z. Zhang, Precipitation of δ phase in inconel 718 superalloy: The role of grain boundary and plastic deformation, Mater. Today Commun. 36 (2023) 106582, http://dx.doi.org/10.1016/j.mtcomm.2023.106582.

[86] Q.L. Her, J. Wong, Significant correlation versus strength of correlation, Am. J. Health Syst. Pharm. 77 (2) (2019) 73–75, http://dx.doi.org/10.1093/ajhp/zxz280.

[87] L. Susmel, D. Taylor, A novel formulation of the theory of critical distances to estimate lifetime of notched components in the medium-cycle fatigue regime, Fatigue Fract. Eng. Mater. Struct. 30 (7) (2007) 567–581, http://dx.doi.org/10.1111/j.1460-2695.2007.01122.x.

[88] L. Herrmann, M. Jokeit, O. Weeger, S. Kollmannsberger, Deep Learning in Computational Mechanics: An Introductory Course, Springer Nature Switzerland, 2025, http://dx.doi.org/10.1007/978-3-031-89529-6.

[89] X. Niu, C. He, S.-P. Zhu, P. Foti, F. Berto, L. Wang, D. Liao, Q. Wang, Defect sensitivity and fatigue design: Deterministic and probabilistic aspects in additively manufactured metallic materials, Prog. Mater. Sci. 144 (2024) 101290, http://dx.doi.org/10.1016/j.pmatsci.2024.101290.

[90] W. Yun, Z. Lu, X. Jiang, L. Zhang, Borgonovo moment independent global sensitivity analysis by Gaussian radial basis function meta-model, Appl. Math. Model. 54 (2018) 378–392, http://dx.doi.org/10.1016/j.apm.2017.09.048.

[91] M. Benedetti, C. Santus, S. Raghavendra, D. Lusuardi, F. Zanini, S. Carmignato, Multiaxial plain and notch fatigue strength of thick-walled ductile cast iron EN-GJS-600-3: Combining multiaxial fatigue criteria, theory of critical distances, and defect sensitivity, Int. J. Fatigue 156 (2022) 106703, http://dx.doi.org/10.1016/j.ijfatigue.2021.106703.

[92] W.-L. Ye, S.-P. Zhu, X. Niu, J.-C. He, J.A.F.O. Correia, Fatigue life prediction of notched components under size effect using critical distance theory, Theor. Appl. Fract. Mech. 121 (2022) 103519, http://dx.doi.org/10.1016/j.tafmec.2022.103519.

[93] M. Benedetti, M. Pedranz, V. Fontanari, C. Menapace, M. Bandini, Enhancing plain fatigue strength in aluminum alloys through shot peening: Experimental investigations and a strain energy density interpretation, Int. J. Fatigue (2024) http://dx.doi.org/10.2139/ssrn.4730379.

[94] L. Makkonen, R. Rabb, M. Tikanmäki, Size effect in fatigue based on the extreme value distribution of defects, Mater. Sci. Eng.: A 594 (2014) 68–71, http://dx.doi.org/10.1016/j.msea.2013.11.045.

[95] A. Ince, G. Glinka, A modification of Morrow and Smith-Watson-Topper mean stress correction models: A modification of Morrow and Smith-Watson-Topper mean stress correction models, Fatigue Fract. Eng. Mater. Struct. 34 (11) (2011) 854–867, http://dx.doi.org/10.1111/j.1460-2695.2011.01577.x.

[96] S.-P. Zhu, Q. Lei, H.-Z. Huang, Y.-J. Yang, W. Peng, Mean stress effect correction in strain energy-based fatigue life prediction of metals, Int. J. Damage Mech. 26 (8) (2016) 1219–1241, http://dx.doi.org/10.1177/1056789516651920.

[97] F. Collini, G. Meneghetti, Towards a fracture mechanics-based fatigue assessment of lattice structures obtained from additive manufacturing of metallic powders, Mater. Des. 244 (2024) 113077, http://dx.doi.org/10.1016/j.matdes.2024.113077.